

Citation for published version:

A. F. McLeod, et al., "A nebular analysis of the central Orion nebula with MUSE", *Monthly Notices of the Royal Astronomical Society*, Vol. 455 (4): 4057-4086, December 2015.

DOI:

<https://doi.org/10.1093/mnras/stv2617>

Document Version:

This is the Published Version.

Copyright and Reuse:

This article has been accepted for publication in *Monthly Notices of the Royal Astronomical Society*.

©:2015 The Authors.

Published by Oxford University Press on behalf of the Royal Astronomical Society. All rights reserved.

Content in the UH Research Archive is made available for personal research or study, educational or non-commercial purposes only. Content is protected by copyright, permissions for further reuse of content should be sought from the publisher, author or other copyright holder.

Enquiries

If you believe this document infringes copyright, please contact the Research & Scholarly Communications Team at rsc@herts.ac.uk

A nebular analysis of the central Orion nebula with MUSE

A. F. McLeod,¹★ P. M. Weilbacher,² A. Ginsburg,¹ J. E. Dale,^{3,4} S. Ramsay¹
and L. Testi^{1,4,5}

¹European Southern Observatory, Karl-Schwarzschild-Str 2, D-85748 Garching bei München, Germany

²Leibniz-Institut für Astrophysik Potsdam (AIP), An der Sternwarte 16, D-14482 Potsdam, Germany

³Universitäts-Sternwarte München, Scheinerstr. 1, D-81679 München, Germany

⁴Excellence Cluster ‘Universe’, Boltzmannstr. 2, D-85748 Garching bei München, Germany

⁵INAF/Osservatorio Astrofisico di Arcetri, Largo E. Fermi, 5, I-50125 Firenze, Italy

Accepted 2015 November 4. Received 2015 November 4; in original form 2015 August 21

ABSTRACT

A nebular analysis of the central Orion nebula and its main structures is presented. We exploit observations from the integral field spectrograph Multi Unit Spectroscopic Explorer (MUSE) in the wavelength range 4595–9366 Å to produce the first O, S and N ionic and total abundance maps of a region spanning 6 arcmin × 5 arcmin with a spatial resolution of 0.2 arcsec. We use the $S_{23} (= ([S\ II] \lambda\lambda 6717, 6731 + [S\ III] \lambda 9068) / H\beta)$ parameter, together with $[O\ II] / [O\ III]$ as an indicator of the degree of ionization, to distinguish between the various small-scale structures. The only Orion bullet covered by MUSE is HH 201, which shows a double component in the $[Fe\ II] \lambda 8617$ line throughout indicating an expansion, and we discuss a scenario in which this object is undergoing a disruptive event. We separate the proplyds located south of the Bright Bar into four categories depending on their S_{23} values, propose the utility of the S_{23} parameter as an indicator of the shock contribution to the excitation of line-emitting atoms, and show that the MUSE data are able to identify the proplyds associated with discs and microjets. We compute the second-order structure function for the $H\alpha$, $[O\ III] \lambda 5007$, $[S\ II] \lambda 6731$ and $[O\ I] \lambda 6300$ emission lines to analyse the turbulent velocity field of the region covered with MUSE. We find that the spectral and spatial resolution of MUSE are not able to faithfully reproduce the structure functions of previous works.

Key words: ISM: abundances – H II regions – ISM: individual objects: M 42 – ISM: jets and outflows.

1 INTRODUCTION

The Orion nebula (M 42) is the closest Galactic H II region and corresponds to one of the most observed objects in the sky. It therefore not only serves as a template for the comparison with observations of other (Galactic and extragalactic) H II regions, but also as a very good testing ground for new instruments. The number of papers written about M 42 in the last six decades is in the three digit regime, demonstrating how important and how well studied this region is. A thorough review of the main features, the geometry, the population of stars, the outflows and the main physical aspects of the H II region conditions is given in O’Dell (2001).

The central part of M 42 is a treasure chest for star formation feedback studies: it is home to four massive stars (one O- and three B-type stars) that make up the so-called Trapezium cluster, of which θ^1 Ori C (of spectral-type O7; Parenago 1954; van Altena et al. 1988) is the most luminous. These stars are ionizing the surrounding material and giving rise to the vast number of detected

nebular emission lines which trace ionization fronts such as the Bright Bar (BB) and the Orion S cloud. Furthermore, because of the ongoing star formation in the region, it hosts many optical Herbig–Haro (HH) and molecular outflows, as well as a large population of young stellar objects called *proplyds* (short for protoplanetary disc; O’Dell & Wen 1994). The three-dimensional structure of this region is that of a blister-like H II region in front of the Orion Molecular Cloud (OMC-1), where the emitting region is ~ 0.1 pc thick and 1 pc in lateral dimension (O’Dell 2001). The most common features of this region are shown in Fig. 1, in an integrated $[S\ II] \lambda 6717$ map.

Because of its vicinity (~ 420 pc; Schlafly et al. 2014), in combination with the fact that it is associated with recent star formation and a comparatively high surface brightness, it is the perfect object to study elemental abundances and therefore help understand not only the chemical evolution of the interstellar medium, but also the process of nucleosynthesis. Many studies have been dedicated to the elemental abundances in the Orion nebula using slit spectroscopy (e.g. Osterbrock, Tran & Veilleux 1992; Esteban et al. 1998; Esteban et al. 2004; Mesa-Delgado, Esteban & García-Rojas 2008), finding that the abundances of heavy elements in Orion are only somewhat higher than solar ones. In the era of integral field

*E-mail amcleod@eso.org

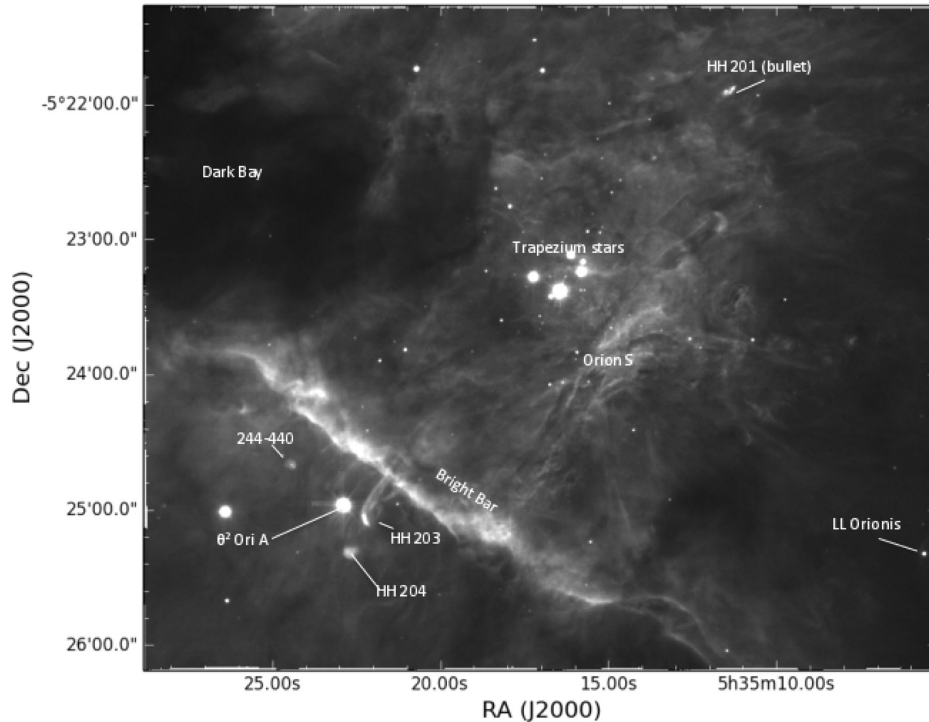


Figure 1. The most commonly discussed features of the central Orion nebula on a MUSE non-continuum subtracted, integrated intensity map of $[\text{S II}] \lambda 6717$.

spectroscopy, new studies have emerged that exploit the combination of simultaneous imaging and spectroscopy on large spatial and spectral scales (e.g. Sánchez et al. 2007; Mesa-Delgado et al. 2011). A common analysis in the study of H II regions is given by line ratios of nebular emission lines which are used as abundance tracers (e.g. $[\text{N II}]/\text{H}\alpha$, $[\text{S II}]/\text{H}\alpha$ tracing the nitrogen and sulphur abundances, respectively) or as tracers of the degree of ionization (e.g. $[\text{O II}]/[\text{O III}]$). Another sulphur abundance parameter computed for both Galactic and extragalactic H II regions is given by $S_{23} = ([\text{S II}] + [\text{S III}])/\text{H}\beta$ (Vilchez & Esteban 1996), which is commonly used to determine star formation histories and evolutionary scenarios, as this parameter is found to vary as a function of position within a galaxy. Together with $[\text{O II}]/[\text{O III}]$, S_{23} can also be used to analyse the ionization structure of H II regions (García-Benito et al. 2010). Together with a spatially resolved velocity map, the combination of the S_{23} parameter and $[\text{O II}]/[\text{O III}]$ has been used by (McLeod et al. 2015, hereafter **MC15**) to detect a previously unknown outflow in the famous Pillars of Creation in the Eagle Nebula (M 16) in MUSE science verification observations, as the location where the outflow is currently emerging from the pillar material has distinctively high S_{23} and low $[\text{O II}]/[\text{O III}]$ values. Future MUSE observations will determine whether this new method can be used to detect outflows in molecular cloud structures. In this work, we exploit this method to characterize the outflow and proplyd population in M 42.

The same nebular emission lines used to determine ionic and total abundances have also been used to study the turbulent motions in M 42 with a statistical approach by computing the second-order velocity structure function, generally defined as $S_2(\mathbf{r}) = \langle |\mathbf{v}(\mathbf{r}') - \mathbf{v}(\mathbf{r}'')|^2 \rangle$ (where $\mathbf{r} = \mathbf{r}' - \mathbf{r}''$ is the separation between any given pair of points), and comparing the shape of the structure function to that of theoretical models of turbulence (e.g. Kolmogorov 1941; von Hoerner 1951). The main studies about structure functions in Orion used the $[\text{O III}]$ (Castaneda 1988), the $[\text{O I}]$ (O'Dell & Wen 1992) and later the $[\text{S III}]$ lines (Wen & O'Dell 1993), which

show that the structure function has a steep slope at small values of r and a transition scale after which the slope is shallower for larger values of r , except for $[\text{O I}]$ where the slope is seen to remain constant over almost all measured scales. In general, the cited studies indicate similarities between the observations and the von Hoerner predictions (see Section 4 and O'Dell 2001).

The new optical integral field unit (IFU) MUSE at the Very Large Telescope offers, for the first time, a very powerful combination of sub-arcsecond spatial resolution and medium spectral resolution over a field of view of $1 \text{ arcmin} \times 1 \text{ arcmin}$ and a large spectral range. With this instrument it is now possible to compute not only ionic and elemental abundance maps, but also compute velocity information from the same observations in an unbiased manner for a very large field. In this work we derive the abundance maps of oxygen, nitrogen and sulphur, analyse how the S_{23} and $[\text{O II}]/[\text{O III}]$ emission line ratios vary across the central part of the Orion nebula and how one can use them to distinguish between the different types of outflows. Furthermore, we attempt a kinematical analysis by computing the second-order structure function. This work demonstrates the potential of IFU spectroscopy to probe different types of feedback mechanisms (ionization, jets/outflows) with a combination of line ratios, kinematics and physical properties. The paper is organized as follows: we briefly present the observations in Section 2, compute and discuss the abundance and line ratio maps of the entire mosaic in Section 3; the structure functions are discussed in Section 4, while in Section 5 we present detailed studies of several selected regions. Finally, the conclusions are presented in Section 6.

2 IFU OBSERVATIONS

The MUSE integral field observations of the Orion nebula were taken during the instrument's commissioning run (Bacon et al. 2014) on 2014 February 16. The $6 \text{ arcmin} \times 5 \text{ arcmin}$ mosaic consists of 60×5 s exposures, where each of the 30 mosaic pointings

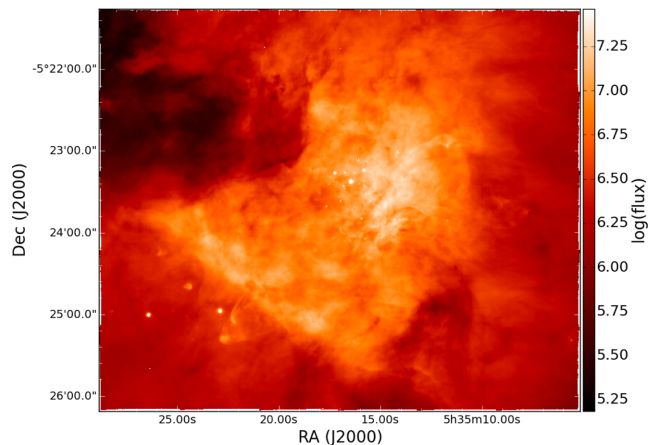


Figure 2. $H\alpha$ continuum-subtracted integrated intensity map, linearly autoscaled (the flux is measured in 10^{-20} erg s^{-1} cm^{-2} $pixel^{-1}$).

was observed twice with a 90 deg rotation dither pattern. The data reduction was carried out in the `ESOREX` environment with the MUSE pipeline (Weilbacher et al. 2012). For a detailed description of the data reduction, we refer to Weilbacher et al. (2015, hereafter W15). The observations were carried out in the wide field mode with a field of view of 1 arcmin \times 1 arcmin, in the wavelength range 4595–9366 Å and a sampling of 0.2 arcsec \times 0.2 arcsec \times 0.85 Å. An integrate intensity map of $H\alpha$ is shown in Fig. 2. Maps of other emission lines, as well as maps of the most relevant physical parameters (e.g. electron density, electron temperature, extinction) are shown and discussed in W15.

3 ABUNDANCE MAPS

3.1 Ionic and total abundances

Abundance determination in the Orion nebula is supported by a long record of publications dating back to the last century (e.g. Peimbert & Torres-Peimbert 1977; Baldwin et al. 1991; Rubin, Dufour & Walter 1993; Esteban et al. 1998; Sánchez et al. 2007; Mesa-Delgado et al. 2011), and it serves as the comparison ground for abundances in other extra- and Galactic $H II$ regions. One of the major problems in determining abundances is the dependence of line emissivity on the electron temperature T_e : the emissivity of recombination lines (RLs) decreases with increasing T_e , while the emissivity of collisionally excited lines (CELs) increases with T_e in an exponential manner (O’Dell 2001). This means that in the case of temperature inhomogeneity along lines of sight (as is the case for Orion; Peimbert 1967) different regions will be more or less sensitive to RLs or CELs, and ratios of RLs are therefore preferentially used to determine abundances because of their weaker dependence on temperature. As the RLs covered by MUSE ($O II_{\lambda 4650}$ and $O II_{\lambda 4661}$) tend to be very weak and noise dominated, in this work we only make use of CEL line ratios to determine abundances.

The large spatial and spectral coverage of MUSE offers the first unbiased possibility of computing ionic abundance maps for many atoms simultaneously. For this, we used integrated intensity maps, corrected for extinction as described in MC15 with $R_V \approx 5.5$, using the `PYTHON` package `PYNEB` together with the electron density and temperature maps derived in W15. The atomic data used for the computations are shown in Table 1. The oxygen abundance ratios O^+/H^+ and O^{++}/H^+ were computed from the $[O II] \lambda\lambda 7320, 7330$ and $[O III] \lambda\lambda 4959, 5007$ lines, respectively, and

Table 1. Atomic data used in `PYNEB` for the ionic abundance determination.

Ion	Transition probability	Collision strength
O^+	Zeippen (1982)	Pradhan et al. (2006)
	Wiese, Fuhr & Deters (1996)	Tayal (2007)
O^{++}	Wiese et al. (1996)	Aggarwal & Keenan (1999)
	Storey & Zeippen (2000)	
S^+	Podobedova, Keller & Wiese (2009)	Tayal & Zatsarinny (2010)
S^{++}	Podobedova et al. (2009)	Tayal & Gupta (1999)
N^+	Galavis, Mendoza & Zeippen (1997)	Tayal (2011)

assuming $T([O II]) \sim T([N II])$ and $T([O III]) \simeq T([S III])$, as MUSE does not cover the $[O II] \lambda\lambda 3727, 3729$ and $[O III] \lambda 4363$ lines to compute $T([O II])$ and $T([O III])$. The $[S II]$ electron density map was used for the abundance determination. The $[O II] \lambda\lambda 7320, 7330$ lines are generally low in intensity and can suffer from the contamination of OH rotational line emission at 7330 Å, and, as stated in W15, the MUSE Orion data cube was not corrected for sky background. However, the nebular emission in the central Orion nebula is very bright compared to the sky, and the maximal contribution of sky emission to the measurements is of 5 per cent to the $[O II]$ lines. Because in the outer regions (e.g. the Dark Bay) the $[O II]$ lines, as well as the $[S II]$ and the $[N II] \lambda 5755$ lines are significantly weaker and the level of noise very high, we masked the emission line maps used to compute the abundance based on the flux of the weakest lines of the three species ($[O II] \lambda 7330 > 4 \times 10^{-16}$ erg s^{-1} cm^{-2} $pixel^{-1}$, $[S II] \lambda 6717 > 4 \times 10^{-16}$ erg s^{-1} cm^{-2} $pixel^{-1}$, $[N II] \lambda 5755 > 4 \times 10^{-17}$ erg s^{-1} cm^{-2} $pixel^{-1}$). The sulphur abundance was computed with $[S II] \lambda 6717$, $[S II] \lambda 6731$ and $[S III] \lambda 9068$, while for nitrogen we made use of the $[N II] \lambda 5755$, $[N II] \lambda 6548$ and $[N II] \lambda 6584$ lines. To account for undetected lines corresponding to higher ionization states we adjust the abundance determination with the appropriate ionization correction factors (ICF), according to Hägele et al. (2008) for sulphur and Esteban et al. (1998) for nitrogen.

The abundance maps are shown in Fig. 3, Fig. 4 and Fig. 5 (the stellar emission has been removed from these maps by fitting and subtracting the continuum on a pixel-by-pixel basis, stars that were saturated appear as white in the images because they are masked out). Mean values for circular regions (with a radius of 2.5 arcsec) of the Trapezium cluster and the BB, as well as of a 8.5 arcsec \times 3 arcsec box as to match the slit Position 2 in Esteban et al. (1998) are shown in Table 2 (to distinguish between our extraction and the actual slit used in Esteban et al. 1998, we label the latter as P2E and the region used for this work as P2). Also shown in the same table are ionic and total abundances obtained by (Esteban et al. 2004, henceforth referred to as E04) for P2.

The total abundance maps computed from the MUSE data show a certain degree of structure: the BB, the Orion S region, the HH 203 and 204 objects, as well as some of the proplyds are clearly seen in the maps. The fact that the abundances are not constant across the nebula but show a certain degree of structure has already been discussed in (Mesa-Delgado et al. 2011, henceforth referred to as MD11) and Núñez-Díaz et al. (2012). Specifically, MD11 find that for the BB their mean value of 8.49 ± 0.03 for the O/H ratio agrees with previous estimates of 8.50 (e.g. Esteban et al. 1998; Blagrove, Martin & Baldwin 2006), that the spatial variation of O/H in the BB varies within the computed typical error, while the range of O/H values is slightly higher for the Orion S region. They also find a coincidence of the lowest O^{++}/H^+ values with the largest electron temperature uncertainties, the highest total oxygen abundance values in spatial agreement with the higher ionic O^+/H^+

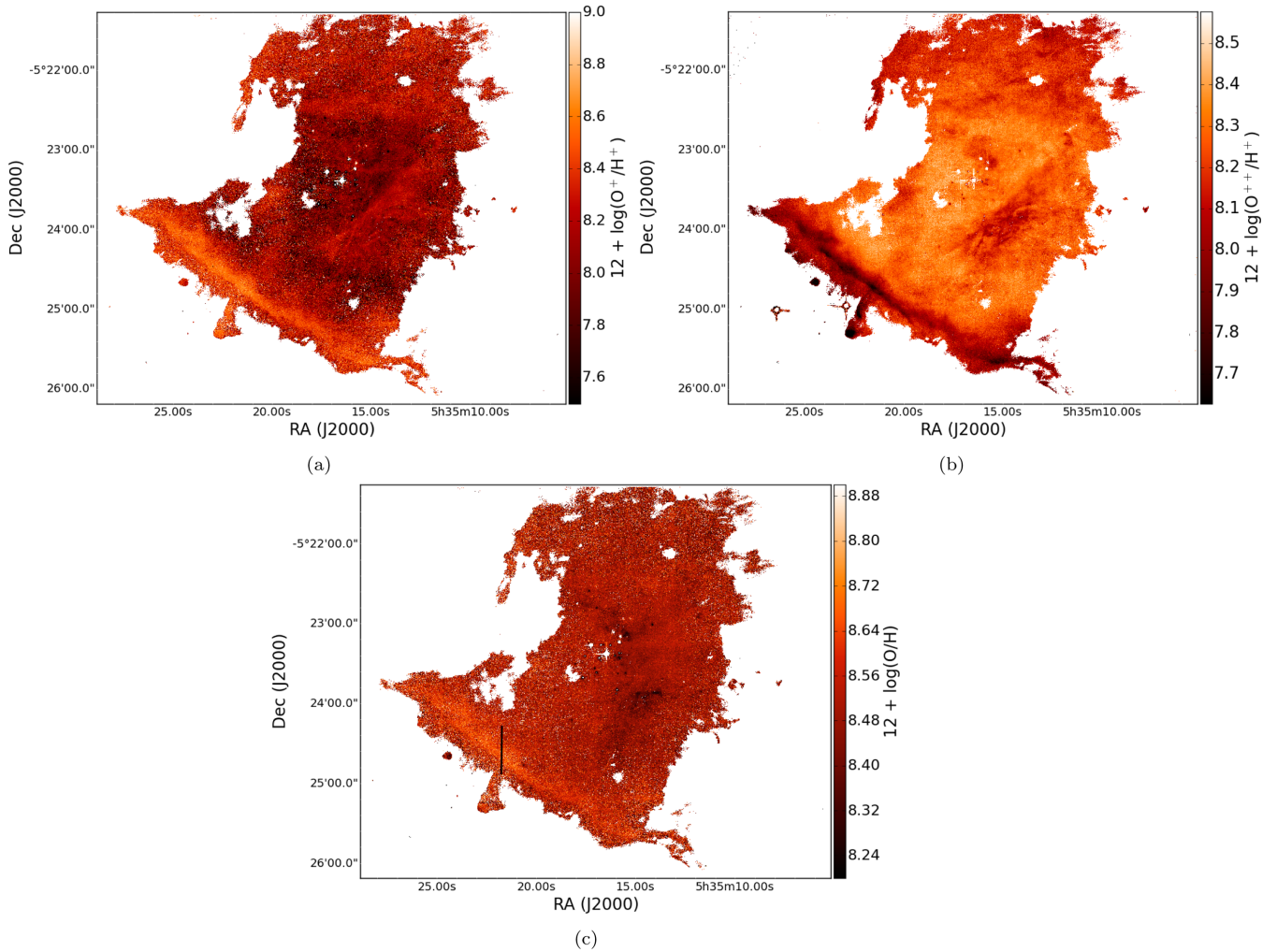


Figure 3. Maps of the O^+ (panel a), O^{++} (panel b) and total O (panel c) abundances, see text Section 3.1. The black line in panel (c) marks the position of the slit used to compute the profiles shown in Fig. 6.

abundance values, and a structural similarity of O^+/H^+ and O/H to the electron density (N_e) map, indicating a strong dependence of the oxygen abundance on the physical parameters. They suggest two possible explanations for this: (i) possibly, the N_e derived from the $[S\ II]$ lines is not appropriate for the determination of O^+/H^+ , as it does not reflect the true density of the O^+ zone; (ii) although reflecting the physical conditions of both S^+ and O^+ , the computed N_e values do not correspond to the true values in regions like the BB or Orion S, as in these regions the density approaches the critical density of the $[S\ II]$ and $[O\ II]$ lines, and higher N_e values are computed. In fact, these authors discuss how, by correcting the N_e to lower values, they recover the mean value for the O abundance. Without any additional information about specifically where to apply such correction, we show uncorrected maps.

To test the reliability of the abundances obtained in this work, we extract a $16\text{ arcsec} \times 16\text{ arcsec}$ sub-region of the BB, matching the observations of MD11. For the entire sub-region, we find a mean O/H ratio of 8.60 ± 0.09 , which is higher than the typical Orion O/H ratio of 8.50. We also compare our temperature, density, O^+/H^+ and O^{++}/H^+ of the sub-region with MD11, and find that our N_e map (derived from the $[S\ II]$ lines) shows: (i) lower values, typically of about $1000\text{--}2000\text{ cm}^{-3}$; (ii) a noise-affected T_e ($[N\ II]$) map; (iii) a comparable O^{++}/H^+ map; (iv) and higher O^+/H^+ as well as O/H

values. We speculate that the higher O^+/H^+ values found for the BB in this work are a result of the noisy T_e and $[O\ II]$ maps. This could be tested with data with higher signal to noise (S/N).

To demonstrate the strong dependence of the ionic and total abundances on the electron density, in Fig. 6 we plot profiles (smoothed with a Gaussian kernel) of these along a slit positioned on the BB (the slit is shown in Fig. 3(c), the profile is computed in direction from north to south): the O^+ and the O abundances show higher values in correlation with the higher N_e values, while the opposite trend is the case for O^{++} . However, we cannot resolve this issue by artificially lowering N_e . Furthermore, the structuring is also seen in S^+/H^+ , N^+/H^+ and N/H : we therefore suggest that the dominant mechanism that leads to the structures seen in the abundance maps is (as already discussed in MD11) that in regions like the BB and the Orion S cloud, densities approach the critical densities of $[S\ II]$, $[N\ II]$ and $[O\ II]$ lead to untrustworthy artefacts.

Table 2 shows that the abundances found in this work do not agree with E04 (Table 3 specifies the electron density and temperatures extracted from the same regions listed in Table 2: for P2 we find a lower N_e as the assumed density of E04, but higher T_e values): in this work, O^+ is overestimated by about 0.22 dex, while O^{++} and O are underestimated by about 0.15 and 0.04 dex, respectively; S^+ is overestimated by 0.16 dex, S^{++} and S are underestimated by

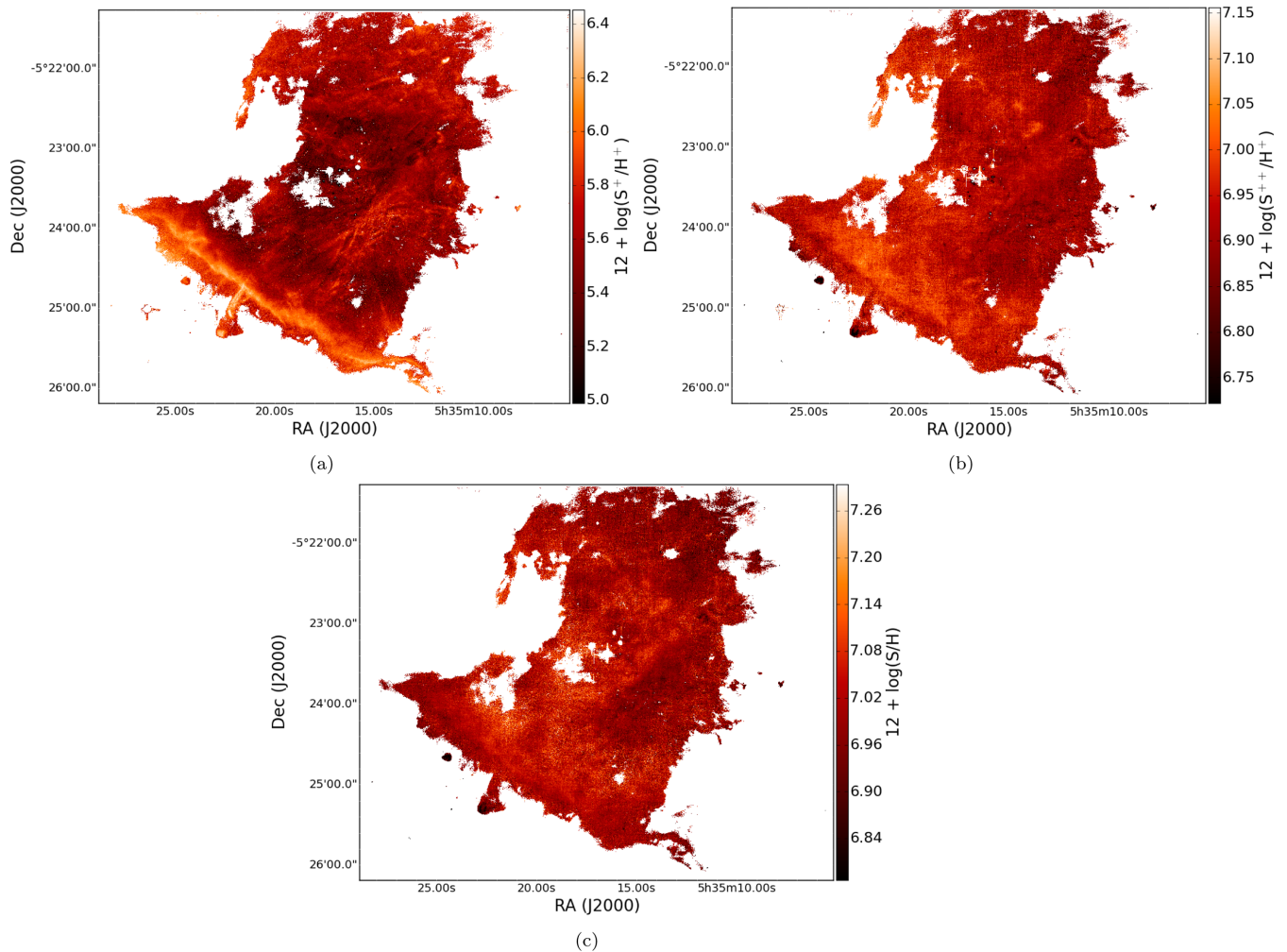


Figure 4. Maps of the S^+ (panel a), S^{++} (panel b) and total S (panel c) abundances, see text Section 3.1.

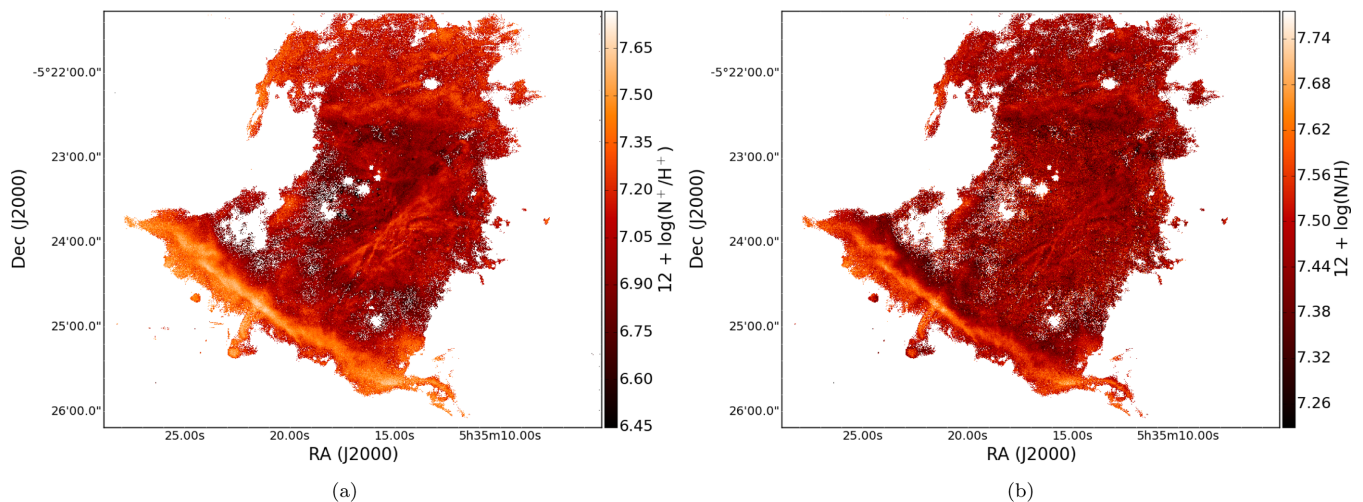


Figure 5. Maps of the N^+ (panel a) and total N (panel b) abundances, see text Section 3.1.

0.09 and 0.04 dex, respectively; for nitrogen, N^+ is overestimated by 0.10 and N underestimated by 0.17 dex. Summarizing this, we see how the abundances computed via `PYNEB` from the MUSE data overestimate the low ionization potential ions (O^+ , S^+ , N^+), and they underestimate the ions with high ionization potential as well

as the total abundances (O^{++} , O, S^{++} , S, N). However, within the margin of errors, the MUSE *total* abundance maps are able to recover literature total O and S abundance measurements. This is not the case for N, as only one ionization state is observed and the total abundance computation relies on the ICF.

Table 2. Ionic and total abundances. Mean values for circular regions with 2.5 arcsec radius centred on selected regions as well as slit position 2 from Esteban et al. (2004), obtained in this work (P2) and abundances computed in Esteban et al. (P2E) for $r^2 = 0.000$. The last line indicates the approximate ranges of abundance values found in MD11 from integral field observations of a sub-region of the BB. See text Section 3.1.

Region	Coordinates (J2000)	O ⁺	O ⁺⁺	O	S ⁺	S ⁺⁺	S	N ⁺	N
BB	5 35 21.91 −5 24 38.20	8.56 ± 0.08	7.93 ± 0.05	8.65 ± 0.06	6.11 ± 0.06	6.98 ± 0.03	7.04 ± 0.03	7.51 ± 0.04	7.60 ± 0.03
Trapezium	5 35 16.4 −5 23 11.9	8.09 ± 0.14	8.31 ± 0.04	8.52 ± 0.06	5.53 ± 0.09	6.92 ± 0.03	7.01 ± 0.04	7.01 ± 0.07	7.44 ± 0.05
P2	5 35 14.54 −5 23 33.86	7.98 ± 0.12	8.28 ± 0.05	8.47 ± 0.04	5.56 ± 0.15	6.92 ± 0.02	7.02 ± 0.03	7.00 ± 0.10	7.48 ± 0.05
P2E, $r^2 = 0.000$	5 35 14.54 −5 23 33.86	7.76 ± 0.15	8.43 ± 0.01	8.51 ± 0.03	5.40 ± 0.06	7.01 ± 0.04	7.06 ± 0.04	6.90 ± 0.09	7.65 ± 0.09
P2-P2E		0.22	−0.15	−0.04	0.16	−0.09	−0.04	0.10	−0.17
MD11	BB	8.00–8.47	7.86–8.24	8.41–8.58					

3.2 Line ratios

In our MUSE observations of pillar-like structures in the Eagle Nebula (see MC15), the $S_{23}(= ([S\ II] \lambda\lambda 6717, 6731 + [S\ III] \lambda 9068)/H\beta)$ parameter was used in combination with $[O\ II] \lambda\lambda 7320, 7330/[O\ III] \lambda 5007$ (as an indicator of the degree of ionization) and a velocity map obtained from the same data set to identify a previously unknown outflow in one of the pillars. However, in MC15 we did not attempt a physical explanation of the empirical fact that S_{23} can be used to trace outflows. Here, we repeated the S_{23} versus $[O\ II]/[O\ III]$ analysis, motivated by the fact that the central Orion nebula hosts a very peculiar combination of massive ionizing stars and a wealth of outflows, forming stars in the form of proplyds, and HH objects. We therefore refine the empirical S_{23} versus $[O\ II]/[O\ III]$ analysis of MC15 by exploring the rich environment of the Orion nebula. Because the relative importance of photoionization and shocks to the production of sulphur emission lines is different for different kind of objects (the Bar, HH outflows and proplyds), it can be used, together with $[O\ II]/[O\ III]$, to distinguish between them (as will be discussed in Section 5.2). The S_{23} map is shown in panel (a) of Fig. 8, panel (b) shows the $[O\ II]/[O\ III]$ map, and panel (c) corresponds to a scatter plot of the two parameters. The maps and scatter plot shown in Fig. 8 are continuum subtracted: the strong stellar residuals of the saturated stars appear as white in the images because it is masked. Furthermore, the white line in Fig. 8(b) shows the slit used to compute the profile shown in Fig. 7 and discussed below.

We applied a technique called *brushing*¹ to analyse the spatial correspondence of the data points in the scatter plot of S_{23} versus $[O\ II]/[O\ III]$ and trace them back to their position in the maps. Both in the $[O\ II]/[O\ III]$ and the S_{23} maps the structures of the nebulosity are clearly distinguishable, e.g. the BB shows high values of both parameters, while the central part of the H II region is marked with lower values of both parameters, meaning that in the vicinity of the Trapezium cluster we find lower S_{23} values and higher degrees of ionization, as is expected.

In Fig. 8(c) S_{23} versus $[O\ II]/[O\ III]$ is shown, and several of the main features are (indicatively) highlighted:² the Orion bullet HH 201 (yellow ellipse) covered by the MUSE field shows high S_{23} values as well as a high degree of ionization, while the proplyds in the vicinity of the Trapezium stars (dark red ellipse) are found

in a region with very low S_{23} values but a rather high degree of ionization; the HH objects and proplyds south of the BB clearly stand out, displaying a wide range in S_{23} and ionization values; furthermore, they can be divided into four distinct classes (described in Section 5.2), marked by the orange, blue, green and cyan ellipses; the BB is marked by the red ellipse.

Fig. 9(a) is a zoom-in on the region of the S_{23} versus $[O\ II]/[O\ III]$ parameter space where most of the data points lie. The $[O\ II]/[O\ III]$ histogram is bimodal, the spatial correspondence of the two distributions is shown in Fig. 9, panels (b) and (c). From this figure, it is clear that the region immediately around the Trapezium stars, as well as the Orion S region, do not show the highest degree of ionization, while the highly ionized matter surrounds these inner regions like a ring. This goes against the naive picture, where matter with the lowest $[O\ II]/[O\ III]$ values (i.e. the highest degree of ionization) should be found in the immediate vicinity of the ionizing stars. The reason for the higher $[O\ II]/[O\ III]$ values is not immediately clear. Because the strong dependence of $[O\ II]/[O\ III]$ on the electron density (as can be seen in Fig. 7, where $[O\ II]/[O\ III]$ and N_e are plotted along the slit marked in Fig. 8b), the following two scenarios can be a possible explanation for this empirical fact:

- (i) density variations: in regions of higher density the ionization parameter is quenched and the emission from low-ionization lines (e.g. $[O\ II]$, $[S\ II]$) enhanced;
- (ii) shocks: the above reasoning for density variations holds if shocks are present as well, as shocks locally compress matter, producing density enhancements.

A further possibility is a combination of these two scenarios, as the central Orion nebula, where the Orion S cloud is located, hosts a wealth of HH outflows and shocks such as HH 529, HH 269, HH 202 (O’Dell 2001).

We will discuss selected sub-regions of the mosaic and the scatter plot in Section 5 in order to disentangle the very large number of data points and distinguish between the different populations.

4 KINEMATICS

Turbulence generates a velocity field characterized by stochastic hierarchical fluctuations, and because of this, a statistical approach such as the second-order structure function has been widely used to analyse turbulent motions in both extragalactic (e.g. Medina Tanco et al. 1997; Lagrois & Joncas 2011) and Galactic (e.g. O’Dell 1986; Wen & O’Dell 1993; Miville-Deschenes, Joncas & Durand 1995; Chakraborty & Anandarao 1999) H II regions. For Orion, this has been done, e.g. with the $[O\ III] \lambda 5007$ line in Castaneda (1988), with the $[O\ I] \lambda 6300$ line in O’Dell & Wen (1992) and with the $[S\ III] \lambda 6312$ line in Wen & O’Dell (1993).

¹ This method was also applied in MC15. It is also known as *graphical exploratory data analysis*, and it allows the user to manually select specific data points from an image or a plot by interactively drawing regions on the latter of the two.

² Because of the large number of data points, we refrained from properly colour-coding single points in the scatter plot and trace them back to their spatial origin in the S_{23} map as was done for HH 201 in Fig. 13.

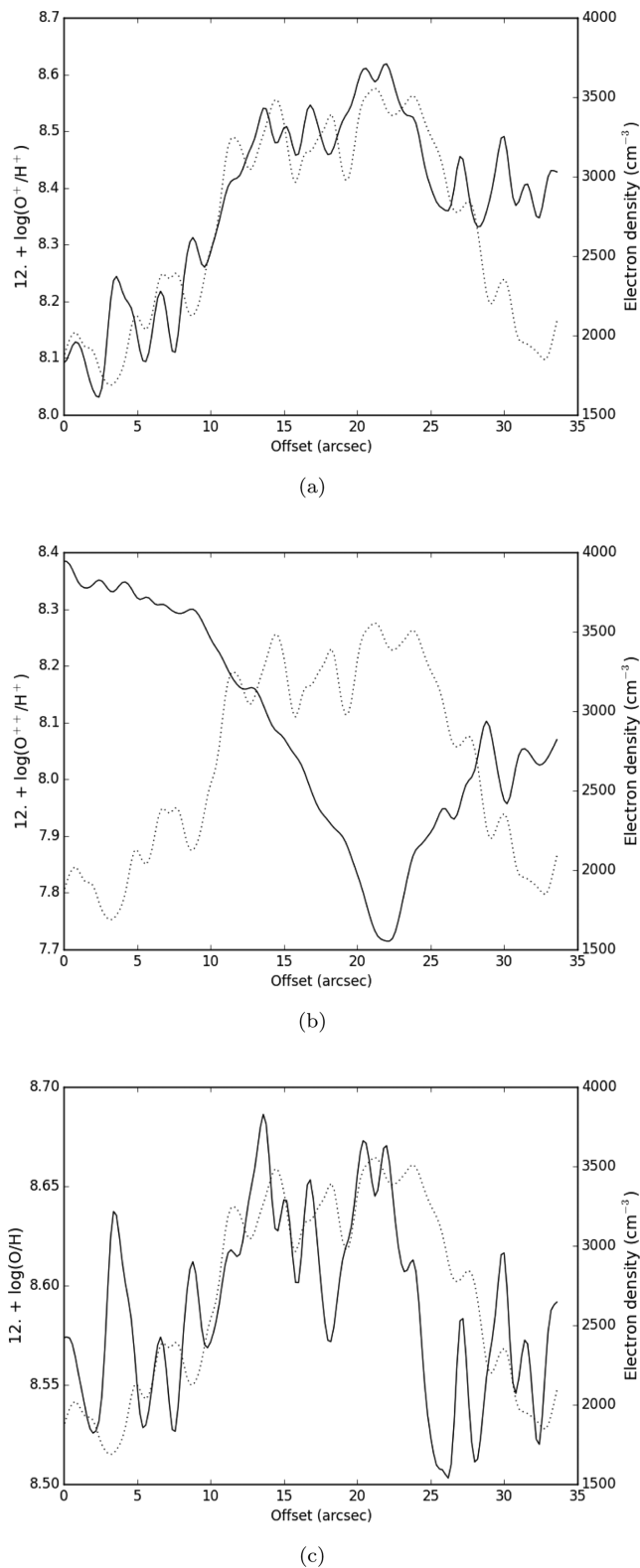


Figure 6. Profiles of the O^+ (top), O^{++} (middle) and O abundances along the slit (along the north–south direction) shown in Fig. 3 (solid lines), together with the profile of the electron density derived from the $[S\text{ II}]$ lines (dotted lines) along the same slit (marked in Fig. 3c). The originally very noisy profiles were smoothed with a Gaussian kernel. See text Section 3.1.

Table 3. Electron densities and temperatures extracted from the same regions listed in Table 2 for this work and slit position 2 in Esteban et. al 2004 (P2E).

Region	N_e ($[S\text{ II}]$) (cm^{-3})	T_e ($[N\text{ II}]$) (K)	T_e ($[S\text{ III}]$) (K)
BB	3430 ± 430	9410 ± 260	8870 ± 190
Trapezium	4530 ± 1080	10090 ± 525	8780 ± 210
P2	7310 ± 3320	10535 ± 520	8950 ± 180
(this work)			
P2E, $r^2 = 0.000$ (Esteban et al. 2004)	8900 ± 200	10000 ± 400	8320 ± 40

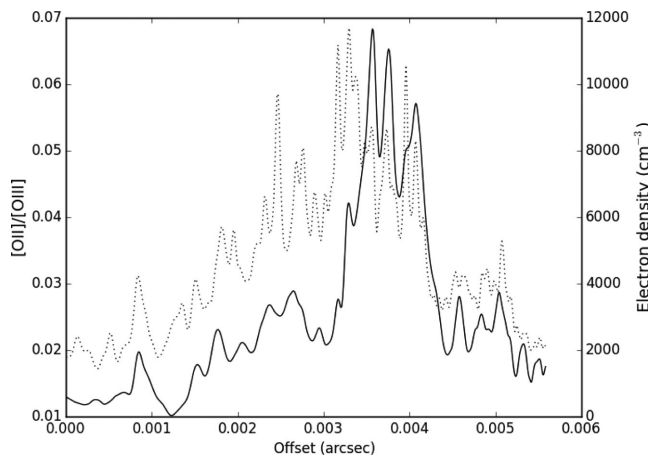


Figure 7. $[O\text{ II}]/[O\text{ III}]$ and N_e along the slit shown in Fig. 8 (see text Section 3.2).

Following the method of Boneberg et al. (2015), we compute the second-order structure function $S_2(\text{d}r)$ as the squared velocity difference between each pair of pixels. As the total number of pixels in the MUSE data set is $> 2 \times 10^6$, we compute the structure function for a randomly selected sample of 10^3 pixels j , around which we radially bin all other pixels i . The size of the random pixel sample was chosen such that the optimum combination between computing time and smoothness was obtained. The structure function then corresponds to the mean of each radial bin,

$$S_2(\text{d}r) = \langle (v_i - v_j)^2 \rangle_{\text{bin}} \quad (1)$$

According to the predictions of von Hoerner (1951), for a homogeneous slab of emitting material of thickness s the structure function should behave as

$$S(r) \propto \begin{cases} r^{n+1} & \text{if } r < s \\ r^n & \text{if } r > s \end{cases}, \quad (2)$$

where $n = 2/3$ in the case of Kolmogorov turbulence. We computed S_2 for the velocity maps of $H\alpha$, $[O\text{ I}] \lambda 6300$, $[O\text{ III}] \lambda 5007$ and $[S\text{ II}] \lambda 6731$. When comparing the shape of S_2 with the velocity map from which each was derived (Fig. 10 and red curves in Fig. 12, respectively), it is clear that for $[O\text{ I}] \lambda 6300$ and $[S\text{ II}] \lambda 6731$ the slope of S_2 is dominated by noise.

In order to quantify the effect of noise on the S_2 slope, we used the MOCASSIN code (Ercolano et al. 2003, 2008; Ercolano, Barlow & Storey 2005) to create synthetic emission line maps from a snapshot of the Run UP simulation of an expanding $H\text{ II}$ region in a turbulent cloud from Dale, Ercolano & Bonnell (2013). We selected a 5×5 pc sub-region of the cloud containing a relatively simple isolated

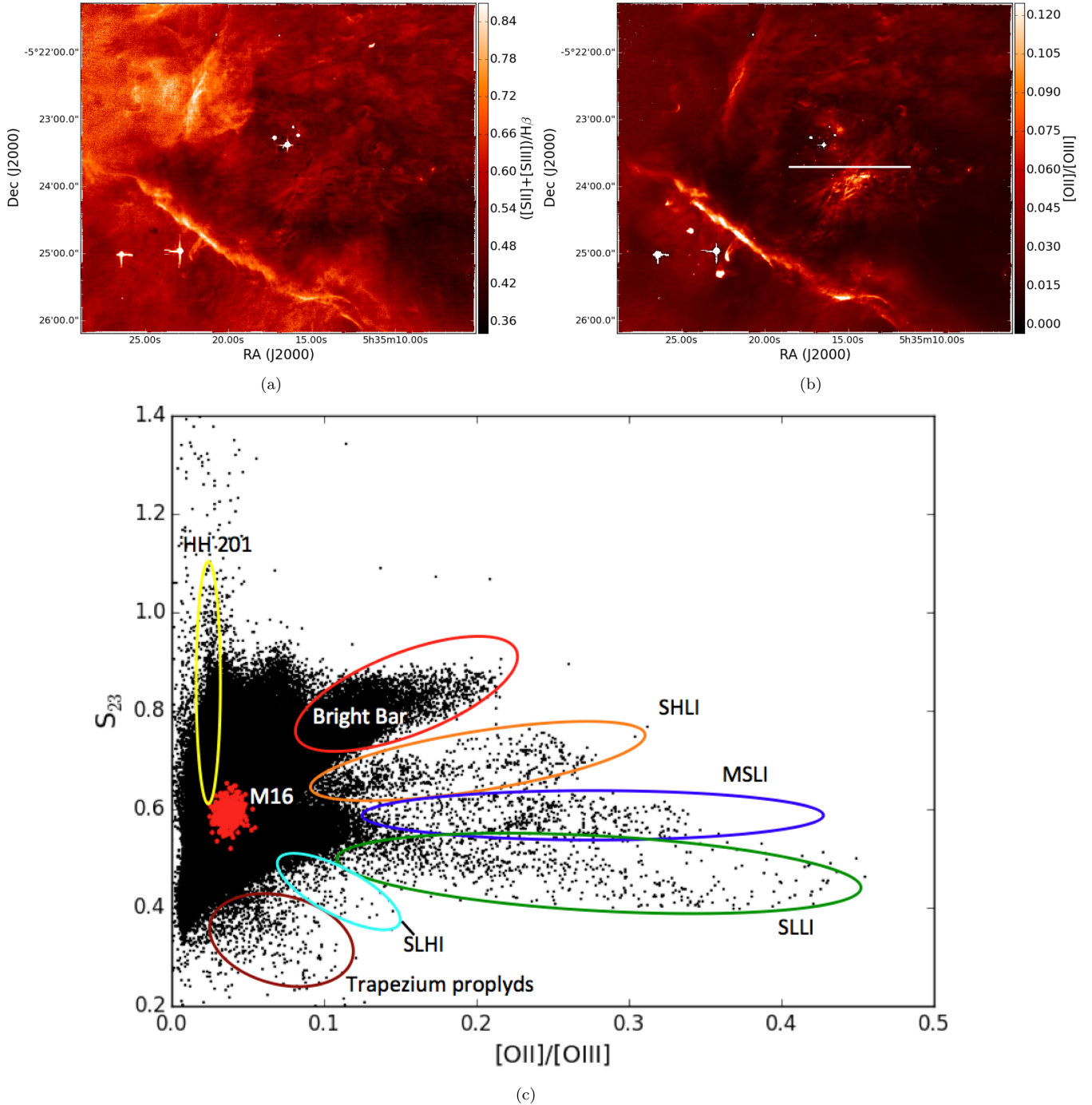
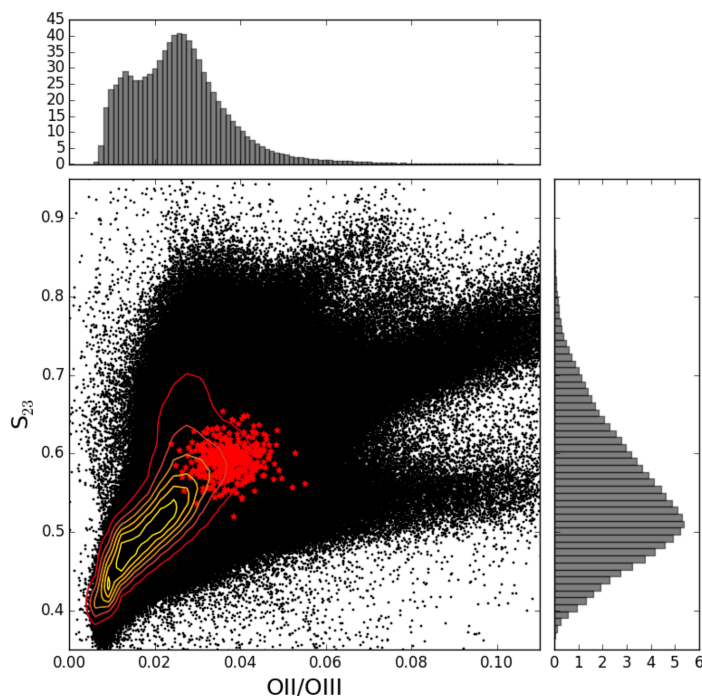


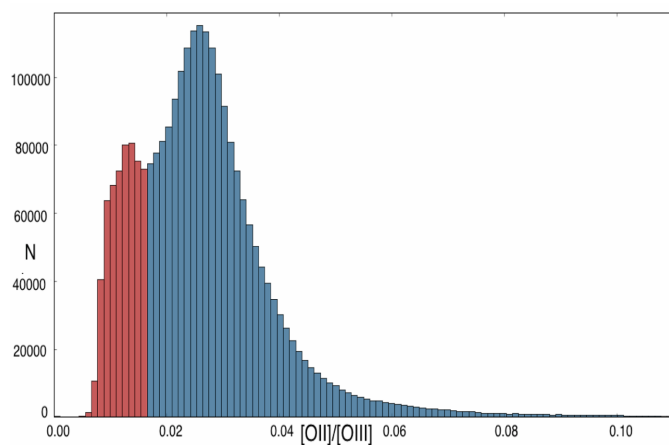
Figure 8. Continuum-subtracted maps of the S_{23} ($=([SII] + [SIII])/H\beta$, panel a) and $[OII]/[OIII]$ (panel b) parameters, linearly scaled. The white line in panel (b) indicates the slit used for Fig. 7. Scatter plot of the two (black points, panel c) and the indicative positions of the following structures: the M 16 outflow (from MC15, red dots), the BB (red), HH 201 (yellow), the proplyds in the Trapezium cluster region (dark red), and the four classes of proplyds and outflows south of the BB (SHLI = S_{23} -high and low ionization, MSLI = medium S_{23} values and low ionization, SLLI = S_{23} -low and low ionization, SLHI = S_{23} -low and high ionization, see text Section 5.2).

bubble, 0.38 Myr after ionization was enabled (see Fig. A6). We then created first-moment maps by convolving the emission line maps with the smoothed-particle hydrodynamics velocity field, as shown in Fig. A2(a). This map has low intrinsic noise, thus it can be used as a baseline. We then added Gaussian noise with increasing values for the standard deviation σ ($\sigma = 0.01, 0.05, 0.1, 0.5, 1, 5, 10$ in panels b–h, not shown are $\sigma = 0.03, 0.15, 0.2, 0.3, 0.75, 2, 3$).

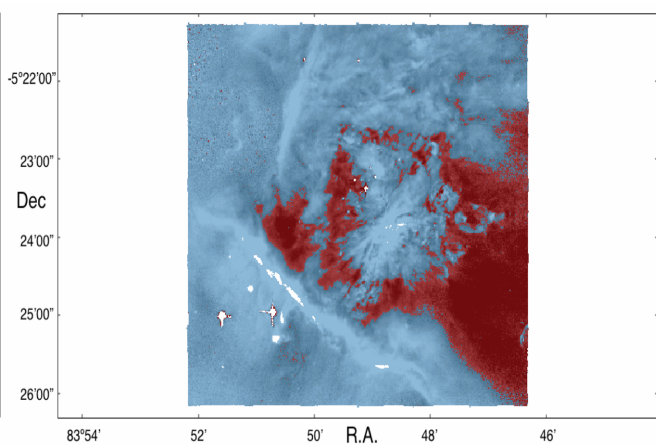
For each of these maps we then computed S_2 , fitted power laws to the resulting structure functions and analysed the dependence of the slope α on σ . The result can be seen in Fig. 11, where a quadratic dependence of the slope on the level of noise is shown. Because of this, we computed a mask based on the intensity of the mean value of the $[O I] \lambda 6300$ line ($\sim 10^{-16} \text{ erg s}^{-1} \text{ cm}^{-2} \text{ pixel}^{-1}$), discarding all pixels below this threshold, and applied this to all the above



(a)



(b)



(c)

Figure 9. Panel (a) zoom-in on the dense region of Fig. 8(c) the contours correspond to the number of data points, the first contour level is $N = 3000$ and the increment is 3000, and the red stars correspond to the M 16 outflow (MC15). The histograms are normalized counts. Panels (b) and (c) illustrate the spatial origin of the bimodal distribution of the $[O\text{II}]/[O\text{III}]$ histogram highest (red) and lower (blue) degree of ionization (the background $[O\text{II}]/[O\text{III}]$ histogram in panel b is the same as at the top of panel a, the red and the blue are the normalized histograms corresponding to the same-shaded areas in panel c). See text Section 3.2.

mentioned velocity maps (see Fig. A1).³ The resulting structure functions are shown in Fig. 12, where S_2 for both the unmasked (red circles) and the masked (blue squares) velocity maps for the four lines are plotted (to visualize the two on the same scale, the ordinate is always normalized to peak). By masking out some of the noise, the slopes of the structure functions are clearly steeper, but because we have no way of effectively getting rid of the noise and therefore computing unbiased structure function slopes both

³ We did not set a higher threshold, as this would have drastically reduced and limited the available length scales.

for the $[S\text{II}]$ and in the $[O\text{I}]$ lines, we concentrate the discussion on the structure functions derived from the $[O\text{III}]$ and the $H\alpha$ lines. These show power-law slopes over all scales, indicating that turbulence is being driven on scales larger than the measured ones, and an energy cascade from the largest scales to the smallest. The slopes however do not correspond to the $2/3$ Kolmogorov law. A comparison of the power-law slopes with previous works shows that the MUSE data, because of a combination of lower spectral resolution, short exposure times and a low S/N ratio (especially for the weaker $[O\text{I}]$ and $[S\text{II}]$ lines), yields structure function slopes that are too shallow with respect to past papers. With high-resolution slit spectroscopy, Castaneda (1988) find a slope of $\alpha \sim 0.86$ for the

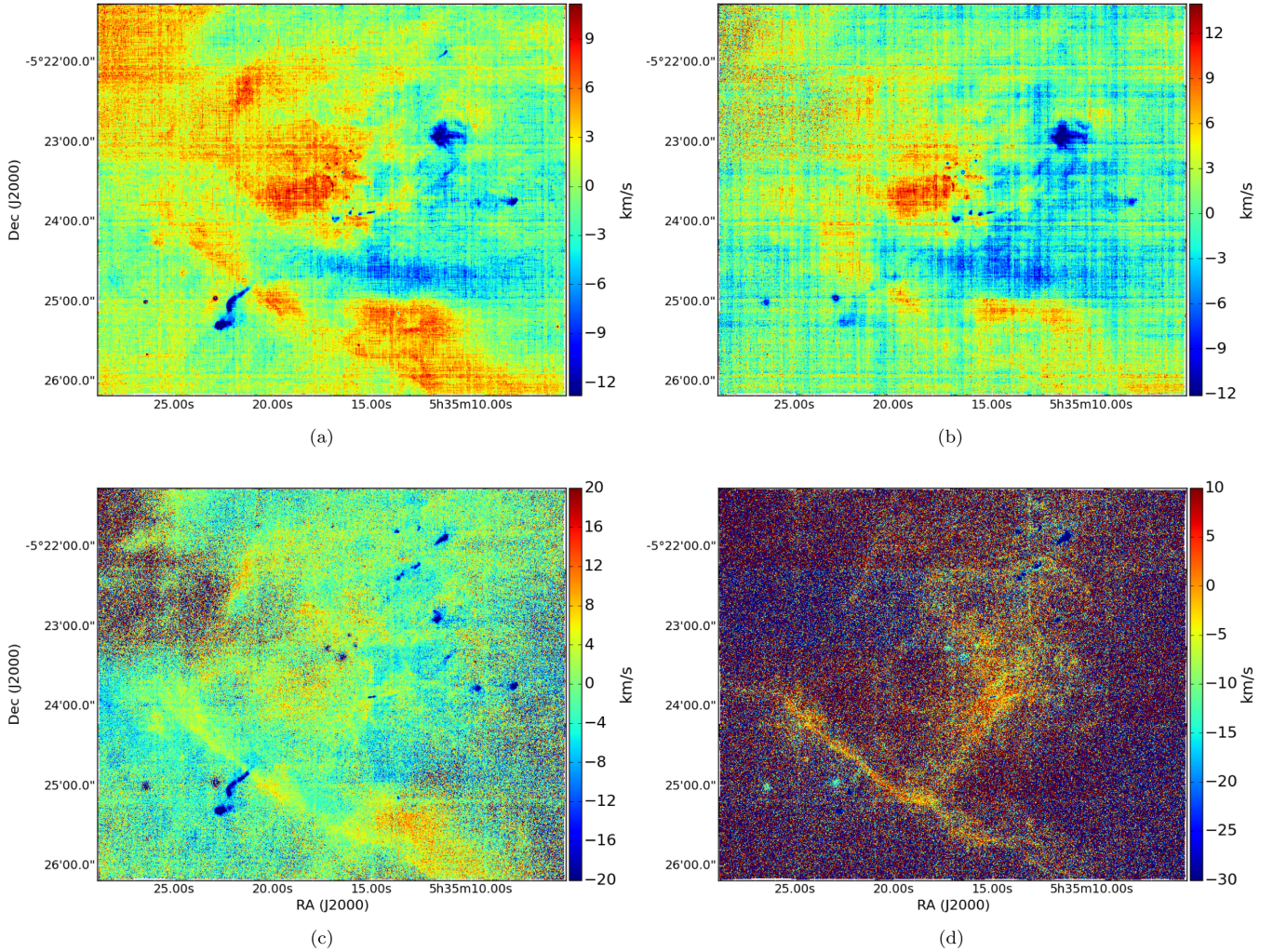


Figure 10. Velocity maps of H α (a), [O III] λ 5007 (b), [S II] λ 6731 (c) and [O I] λ 6300 (d). The indicated velocities correspond to velocities relative to the mean velocity (see text Section 5.1).

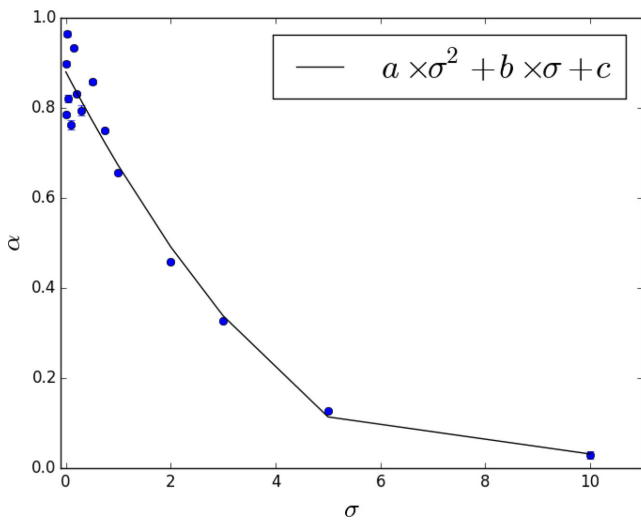


Figure 11. The slopes α resulting from a least-square fit to the of the structure functions computed from the [S II] maps of our simulated H II regions as a function of Gaussian noise with gradually increasing σ . The error bars correspond to the errors from the least-square fit (see text Section 4). A quadratic function was fitted with coefficients $a = 0.0143 \pm 0.0020$, $b = -0.2285 \pm 0.0193$, $c = 0.8922 \pm 0.0208$.

[O III] λ 5007 line, which is a factor of about 2.6 steeper than $\alpha \sim 0.29$ found in this work. For the [O I] λ 6300 line, O'Dell & Wen (1992) find an almost exact Kolmogorov slope of 2/3, while we are completely noise dominated and find $\alpha \sim 1$. What we also do not recover from the MUSE observations is a break in the power-law slopes as was previously found in the above-mentioned studies. We will discuss the influence of noise on simulated structure functions in further detail in McLeod et al. (in preparation). It is however of importance to state the implications of these results, should they be correct: a structure function slope that does not show a break hints at a uniform injection of turbulence on all observed scales (and that turbulence is injected at larger scales than the observed), while the fact that it is shallower than Kolmogorov indicates that the injected turbulence is not sufficient to maintain a Kolmogorov-type velocity field.

5 DISCUSSION OF SELECTED REGIONS

5.1 The Orion bullet HH 201

The only feature that, because of its very high S_{23} values, stands out in the S_{23} map shown in Fig. 8(a) is one of the so-called Orion bullets in the upper-right corner of the image, in fact the only bullet

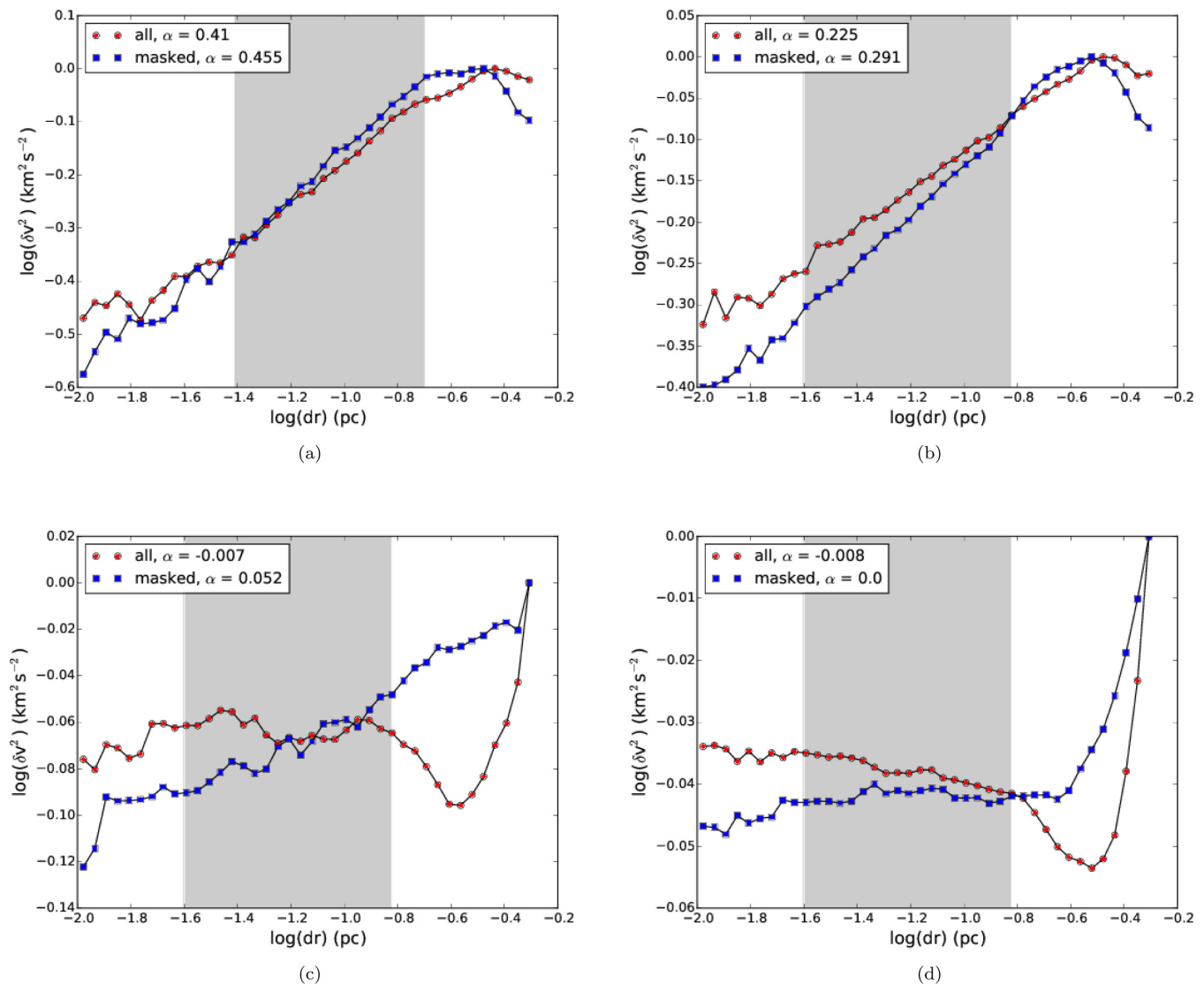


Figure 12. Structure functions (normalized to peak) of $H\alpha$ (a), $[O\text{ III}]\ \lambda 5007$ (b), $[S\ \text{II}]\ \lambda 6731$ (c) and $[O\ \text{I}]\ \lambda 6300$ (d). The red circles are computed from the full velocity maps, the blue squares from the masked ones. The shaded areas correspond to the least-square fitting range used to compute the slope α . See text Section 4.

covered by the MUSE field. This object corresponds to HH 201 (Graham, Meaburn & Redman 2003), a bright shock from an outflow driven by the high-mass star-forming region OMC-1 (Bally, O’Dell & McCaughrean 2000). To better analyse this region, we cropped the original mosaic to a $32\ \text{arcsec} \times 20\ \text{arcsec}$ rectangle (centred at RA J2000 = $5^{\text{h}}35^{\text{m}}11^{\text{s}}.179$, Dec J2000 = $-5^{\circ}21'57''.22$), as to cover both the bullet and a representative portion of the surrounding material. Just like the outflow detected in M 16 (see MC15), the bullet corresponds to a population in the S_{23} versus $[O\ \text{II}]/[O\ \text{III}]$ parameter space (Fig. 13b) that clearly deviates from the rest. This population, just as the M 16 outflow (red stars in Fig. 8c), displays very high S_{23} values, as well as a relatively high degree of ionization, but compared to the M 16 outflow, HH 201 has S_{23} values higher by a factor of ~ 1.5 . Not only does HH 201 show higher S_{23} values than the M 16 outflow, it also shows a higher degree of ionization. This is not surprising, as the low-velocity M 16 outflow most probably originates from a deeply embedded protostar, and the outflow itself is just now emerging from the pillar material where the driving source is embedded; HH 201 on the other hand is

a high-velocity outflow travelling in a less dense medium, it originates from a highly energetic explosive event (Bally et al. 2015a) rather than a protostar and it is closer (in projection) to the ionizing O-star.

The integrated intensity maps of $[O\ \text{I}]\ \lambda 6300$, $[S\ \text{II}]\ \lambda 6717$, $[O\ \text{II}]\ \lambda 7320$, $[N\ \text{II}]\ \lambda 6584$, $H\alpha$ and $[O\ \text{III}]\ \lambda 5007$ (Figs 14a–f, due to an imperfect continuum-subtraction, the residual of a star in the right-hand side of the images is seen) show that the contrast between the bullet and the surrounding medium gets weaker as a function of the ionization state. The sharpest contrast is seen in the neutral $[O\ \text{I}]\ \lambda 6300$ line, whereas the $[O\ \text{III}]\ \lambda 5007$ map only shows diffuse emission. The velocity maps of the same emission lines (Fig. 15) show a similar behaviour: the bullet can be clearly identified in the $[O\ \text{I}]$ and $[S\ \text{II}]$ maps, where it assumes a blueshifted cometary shape with a head pointing away from the Trapezium cluster and a tail pointing back towards it. In the $[O\ \text{II}]$ velocity map only the head can be identified as being slightly blueshifted, while the bullet cannot be seen at all in the $[O\ \text{III}]$ map. Furthermore, the $[O\ \text{I}]$ and $[S\ \text{II}]$ maps reveal a clear velocity difference between the head and the tail of

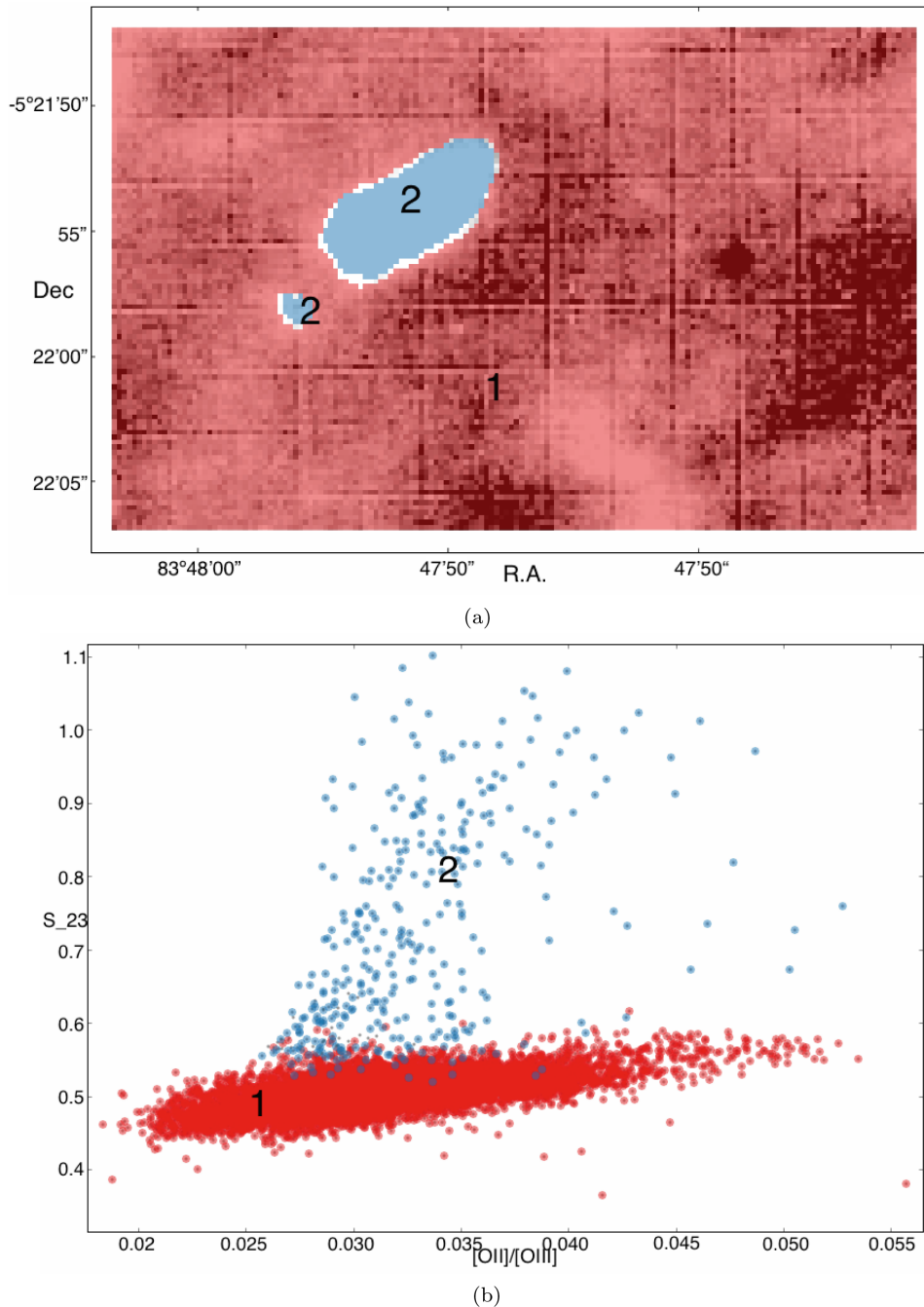


Figure 13. S_{23} map of the Orion bullet covered by MUSE (panel a), colour-coded according to the S_{23} versus $[O II]/[O III]$ plot in panel (b) H II region (red circles, number 1) and the bullet (blue circles, number 2).

about 50 km s^{-1} , the head showing the more negative velocities. The head–tail geometry and the velocity difference between the two could be the result of the high-velocity bullet ramming into a high-density region and being slowed down by the impact. The velocities reported here correspond to relative velocities, meaning that for each line we subtracted the mean velocity of the surrounding medium from the entire velocity map.

The Orion bullets are particularly bright in emission lines of ionized iron (Bally et al. 2015b; Youngblood et al. in preparation), and the near-infrared $[Fe II]$ line (at $1.644 \mu\text{m}$) profiles of HH 201 appear to be consistent with theoretical predictions of a bow shock (Tedds, Brand & Burton 1999). We inspected the line profile of the

brightest of the detected iron lines, $[Fe II] \lambda 8617$, and find a double component throughout the head of the bullet and along its tail. This can be seen in Fig. 16, where the continuum-subtracted and Gaussian-fitted spectra for eight pixels are shown, together with the integrated $[Fe II] \lambda 8617$ intensity map (central panel). Where only one component is seen (not shown in Fig. 16), the typically line width is $\sim 300 \text{ km s}^{-1}$, while for in case of a double-peaked line the FWHM is $\sim 30\text{--}45 \text{ km s}^{-1}$ for the red component and $\sim 20\text{--}60 \text{ km s}^{-1}$ for the blue component. The blue component is typically lower in intensity than the red one. Table 4 shows the best-fitting centroid and width values obtained with PYSPECKIT, using a two-component Gaussian fit.

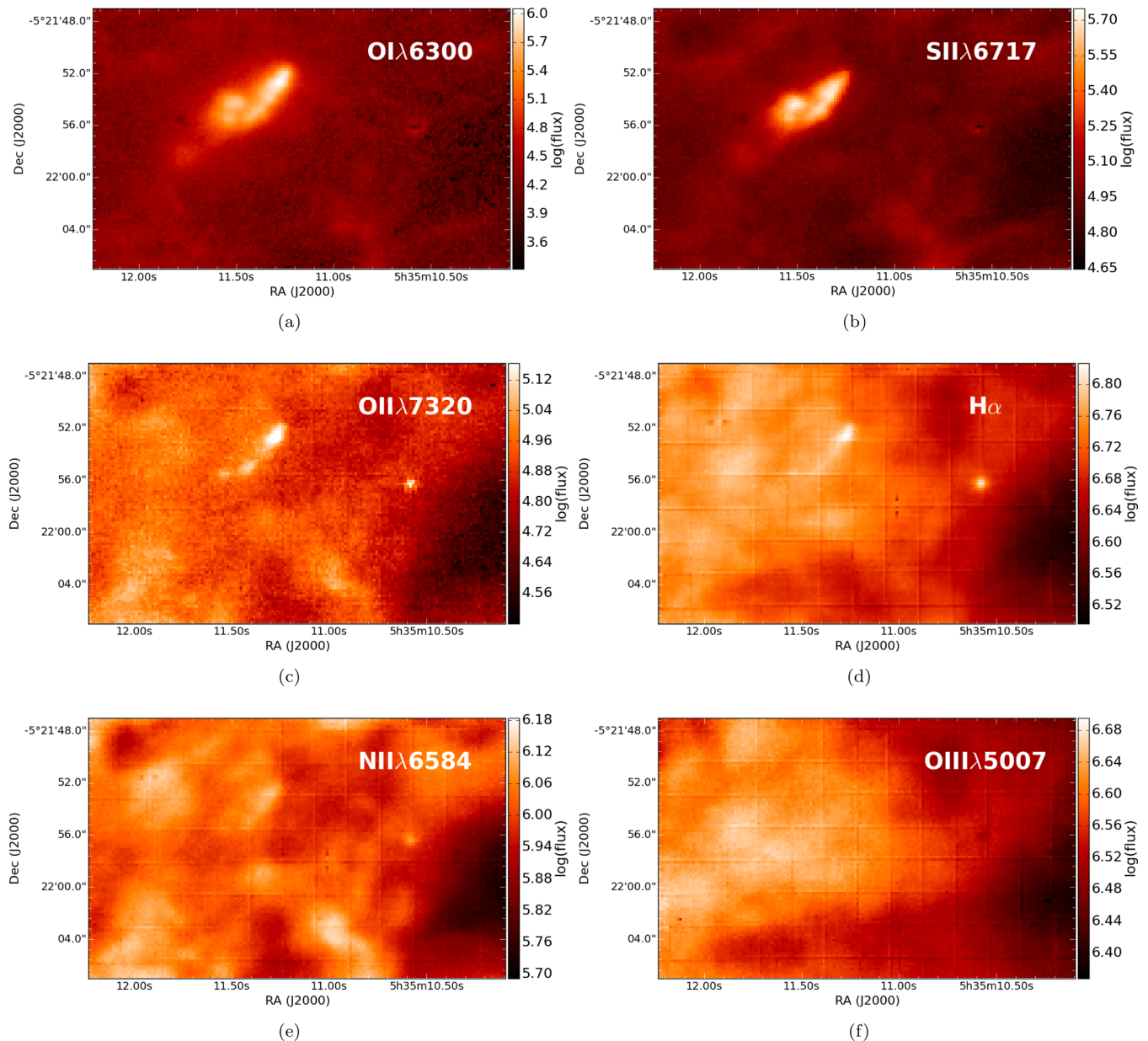


Figure 14. Continuum-subtracted and extinction corrected, integrated intensity maps of the Orion bullet covered by MUSE [O I] $\lambda 6300$ (a), [S II] $\lambda 6717$ (b), [O II] $\lambda 7320$ (c), $\text{H}\alpha$ (d), [N II] $\lambda 6584$ (e) and [O III] $\lambda 5007$ (f). The flux is measured in $10^{-20} \text{ erg s}^{-1} \text{ cm}^{-2} \text{ pixel}^{-1}$, all maps are linearly scaled to minimum/maximum. Residual stellar emission from the continuum subtraction can be seen at RA $5^{\text{h}}35^{\text{m}}10^{\text{s}}.583$, Dec $-5^{\circ}21'56''.50$ (J2000).

We interpret the detection of two velocity components along the line of sight as a sign of expansion. For the evolutionary scenario of this bullet we therefore suggest that it is currently being disrupted, probably because of it being a high-velocity and high-density object hydrodynamically interacting with the surrounding Orion nebula, for example by impacting on a high-density region.

5.2 Outflows and proplyds

In terms of the S_{23} versus [O II]/[O III] analysis, the region just south of the BB containing the HH objects 203 and 204, as well as several of the Orion proplyds including Orion 244-440, is of great interest. The proplyds on this side of the Bar occupy a completely different region in Fig. 8(c) than the proplyds that lie on the other side of the Bar and that are under the direct influence of the Trapezium stars.

This is not surprising, as the physical conditions in the two regions differ in terms of ionizing radiation and other feedback mechanisms (like stellar winds and outflows), which lead to the proplyds south of the Bar having higher S_{23} values and displaying lower degrees of ionization. A $1.2 \text{ arcmin} \times 1.0 \text{ arcmin}$ sub-cube was generated so to analyse this region in more detail, integrated intensity maps of [O I], [S II], [O II], $\text{H}\alpha$, [N II] and [O III] are shown in Fig. 17.

Fig. 18(b) shows the colour-coded S_{23} versus [O II]/[O III] parameter space, as well as the corresponding S_{23} map (panel a). The S_{23} versus [O II]/[O III] parameter space separates the various objects in this field into different populations: the Bar shows higher S_{23} values than the proplyds and HH objects, while these show a wider range of degrees of ionization. The clear separation into different populations however is not seen when considering [S II]/ $\text{H}\beta$ (or [S II]/ $\text{H}\alpha$) as is shown in Fig. A7, where the same populations are not as clearly

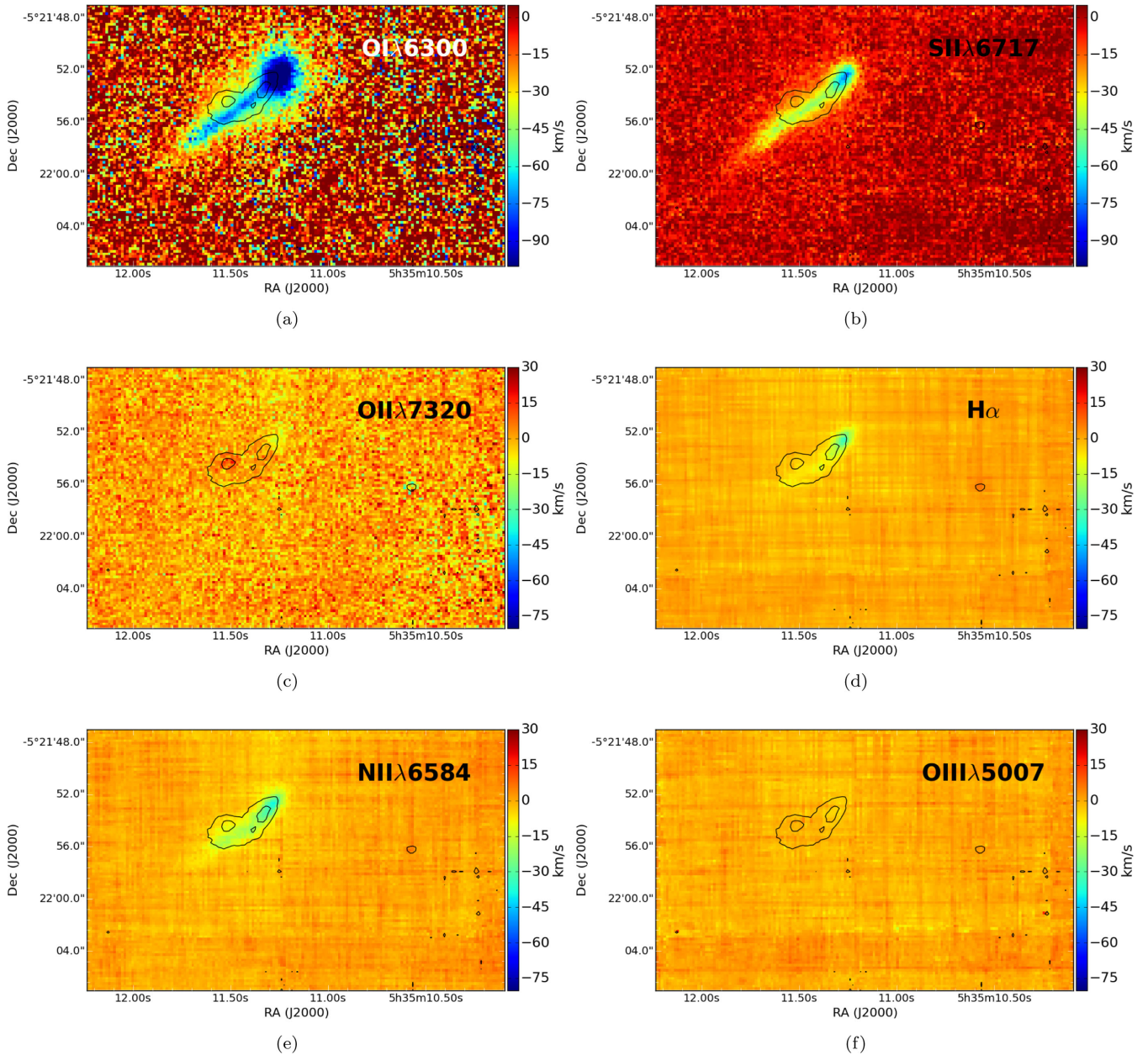


Figure 15. Velocity maps of the Orion bullet covered by MUSE [O I] $\lambda 6300$ (a), [S II] $\lambda 6717$ (b), [O II] $\lambda 7320$ (c), $H\alpha$ (d), [N II] $\lambda 6584$ (e) and [O III] $\lambda 5007$ (f). Black contours correspond to S_{23} values (at RA $5^{\text{h}}35^{\text{m}}10^{\text{s}}.583$, Dec $-5^{\circ}21'56''.750$ a residual from the continuum-subtraction is seen). The indicated velocities correspond to velocities relative to the mean velocity of the surrounding medium (see text Section 5.1).

separated and overlapping. We interpret this as S_{23} being an indicator of the relative contribution of shocks (and photoionization) to the excitation of the sulphur atoms, as shocks locally compress matter, reducing the ionization parameter and therefore enhancing the emission of low- over high-ionization species (e.g. enhancing [S II] emission with respect to [S III]). In this scenario, the Bar shows higher S_{23} values because photoionization from the Trapezium stars produces a larger fraction of [S III] emission, which is not the case for the objects south of the Bar.

We cross-matched the identified sources in this field with the *HST*/ACS Atlas of Great Orion nebula proplyds (Ricci, Robberto & Soderblom 2008), and report their main characteristics in Table 5, where the types are i = ionized disc seen in emission, J = jet, B = binary system (from Ricci et al. 2008), and mj = microjet (from

Bally et al. 2000). All of the proplyds in this field are associated with ionized discs seen in emission, and in general the objects can be separated into four classes, depending on their S_{23} values and degree of ionization:

- (i) S_{23} -low and high ionization (*SLHI*): proplyds *a*, *c*, *d*, *j* and outer layer of HH 204,
- (ii) S_{23} -low and lower ionization (*SLLI*): proplyds *c* and *d*,
- (iii) mean S_{23} values and lower ionization (*MSLI*): HH 204, proplyds *j*, *c* and *l*,
- (iv) S_{23} -high and lower ionization (*SHLI*): proplyds *b*, *f*, *g*, *h*, *i* and *n*, tip of HH 203, HH 204.

The proplyd 232-455 (indicated with the letter *m* in Fig. 18a) is a non-detection in our data, as the emission is dominated by the

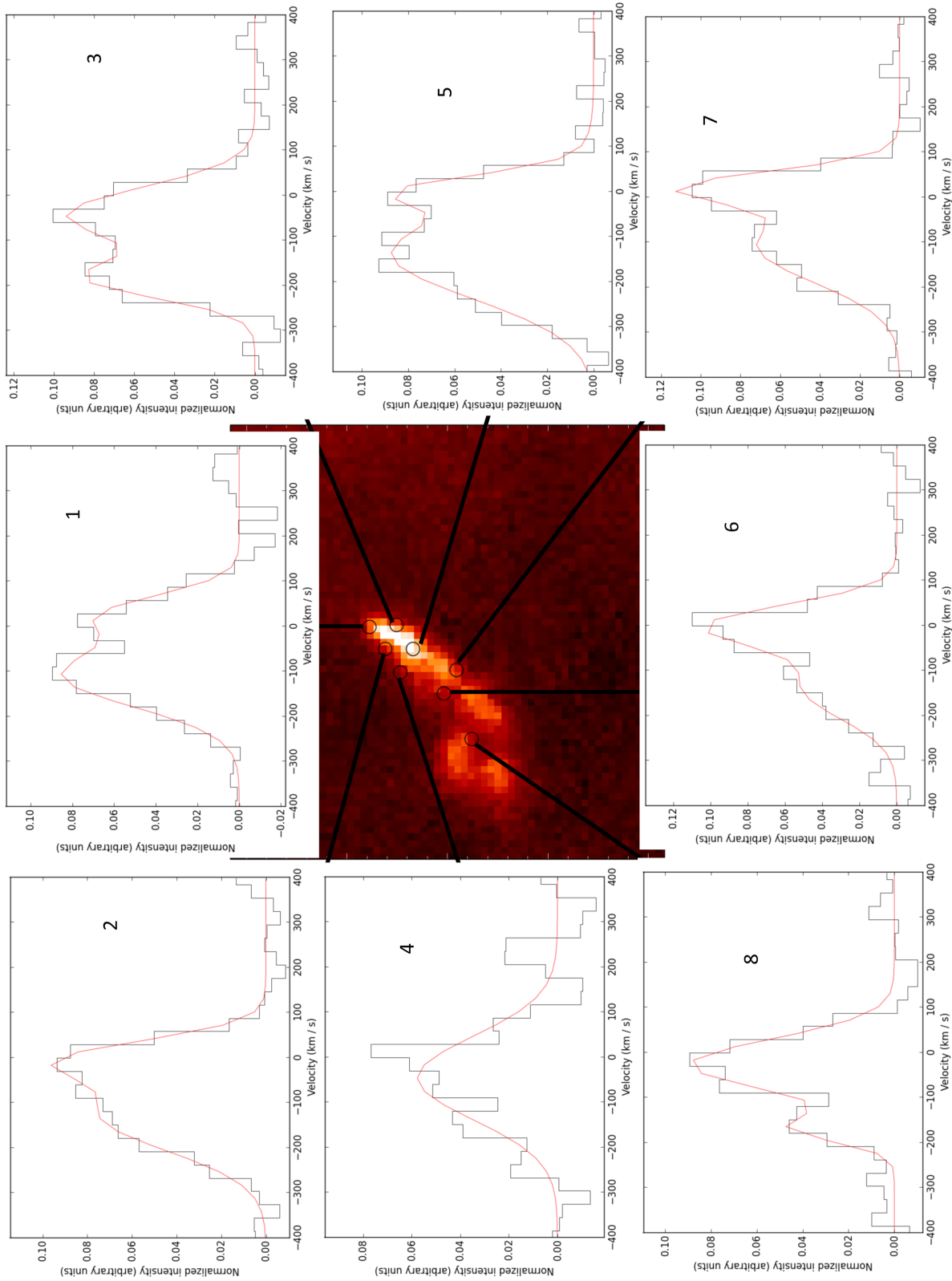


Figure 16. Integrated intensity map of the [Fe II] $\lambda 8617$ line (middle), and the spectra corresponding to the pixels marked by the centroid of the black circles. The spectra are continuum subtracted, and fitted with a two-component Gaussian (the numbers correspond to the entries in Table 4, see also text Section 5.1 for details).

Table 4. Best-fitting parameters of the Gaussian fitting to the [Fe II] $\lambda 8617$ lines shown in Fig. 16. Centroids and widths are measured in km s^{-1} , values are rounded to the nearest integer.

Position (J2000)	Coordinates (blue)	Centroid (blue)	Width (red)	Centroid (red)	Width
1	5 35 11.29 –5 21 52.15	-108 ± 12	69 ± 10	29 ± 11	43 ± 9
2	5 35 11.25 –5 21 52.49	-126 ± 28	80 ± 20	-25 ± 10	42 ± 11
3	5 35 11.34 –5 21 52.60	-186 ± 10	42 ± 8	-44 ± 11	61 ± 10
4	5 35 11.29 –5 21 52.98	-46 ± 12	92 ± 12	–	–
5	5 35 11.25 –5 21 51.68	-138 ± 11	99 ± 10	4 ± 5	32 ± 8
6	5 35 11.38 –5 21 53.90	-136 ± 30	70 ± 24	0 ± 10	46 ± 7
7	5 35 11.34 –5 21 54.28	-107 ± 11	-30 ± 8	-27 ± 5	57 ± 6
8	5 35 11.47 –5 21 54.73	-168 ± 12	69 ± 10	29 ± 11	43 ± 9

ghost of θ^2 Ori A. Not in the Ricci et al. catalogue is the object indicated with the yellow triangle (object *n*) in Fig. 18(a), which is found just below HH 203. We tentatively classify this source as a candidate proplyd and assign it the identifier 224-510, as it displays similar S_{23} and $[\text{O II}]/[\text{O III}]$ values as the objects in the SHLI category, but was not detected by Ricci et al. and we do not have the spatial resolution of *HST* to better resolve the source and an eventual microjet/outflow. We will now briefly discuss the objects belonging to the four classes.⁴

5.2.1 Multiclass objects: HH 204 and Orion 244-440

Both HH 204 and Orion 244-440 seem to have S_{23} -high as well as S_{23} -low components, but while 244-440 appears to have a layered structure, HH 204 shows a *head-tail* configuration. Orion 244-440 is a giant proplyd containing a young stellar object, or possibly even a binary system, with a one-sided microjet along the north-east axis (Bally et al. 2000). Figs 18 and A8 (panels c and d) show that the outer layer of 244-440 appears to be S_{23} -low over a wide range of $[\text{O II}]/[\text{O III}]$, while the inner part, corresponding to the star+disc component of the proplyd (magenta box marked with the letter *c* in Fig. 18), shows a steep rise in S_{23} values. Complementary to Henney & O’Dell (1999), we provide a sketch of Orion 244-440 in Fig. 19: the outer, S_{23} -low, layer of the proplyd, shows a positive $[\text{O II}]/[\text{O III}]$ outside-in gradient, confirming the model of Henney & O’Dell where the ionized density of the outer layers is low, and increases when moving in towards the proplyd; the star+disc component seems to be aligned with the direction towards θ^2 Ori A and the direction of motion (indeed, O’Dell, Wen & Hu 1993 find that some proplyds are oriented towards θ^2 Ori A, rather than θ^1 Ori C). The star+disc component itself is characterized by an S_{23} gradient that increases in the direction of motion.

The head of HH 204 (sketched in Fig. 20 and highlighted in Fig. A8, panels a and b), on the other hand, displays intermediate S_{23} values, and a S_{23} -low tail that shows an ionization front in the direction of θ^2 Ori A. Also, just as 244-440, it covers a broad range of $[\text{O II}]/[\text{O III}]$, and because of its layered structure it belongs to more than one of the four classes.

Núñez-Díaz et al. (2012) performed a thorough analysis of HH 204 with integral field data from the Potsdam Multi-Aperture

Spectrograph. They find a clearly stratified ionization structure across HH 204, and discuss the presence of a trapped ionization front at the head of the bow shock, due to the a high $[\text{O I}]/\text{H}\beta$ ratio at that position, on the opposite side of the source of ionization. In their analysis, the location of the enhanced $[\text{O I}]/\text{H}\beta$ ratio is also characterized by an enhanced $[\text{S II}]/\text{H}\beta$ ratio, which is in good agreement with the enhanced S_{23} found in this work at the head of the bow shock (marked as SHLI in Fig. 20).

5.2.2 SHLI: HH 203, proplyds 239-510, 242-519, 247-436 and the candidate proplyd 224-510

All of these objects are classified under SHLI, but they can be further separated into two sub-classes, depending on the presence of a microjet or not. The object HH 203 appears to have a different structure in terms of the S_{23} parameter than HH 204, and only its tip deviates from the general cluster of data points in Fig. 18(b) that originate from the ambient matter. Its tip classifies as SHLI, as does proplyd 239-510 and the candidate proplyd (identified as *h* and *n*, respectively in Table 5 and Fig. 18a). Also classified as SHLI are the proplyds 247-436 and 242-519 (*b* and *i*, respectively), but these two are associated with microjets (Bally et al. 2000): indeed, although SHLI are limited by spatial resolution, we seem to be able to distinguish two components in these two proplyds, corresponding to a stellar and an outer (shell-like) component (marked in red and green, respectively, in Figs A8a, b and Figs A11a, b).

5.2.3 SLHI: proplyds 250-439, 252-457 and 236-527

These three proplyds (identified as *a*, *d* and *j*, respectively, in Table 5) occupy the S_{23} -low but highly ionized region of the scatter plot. Of the three, only 252-457 is associated with a particularly long jet of about 15 arcsec, more details are discussed in Bally et al. (2000).

5.2.4 SLLI and MSLI: proplyds 245-502 and 206-446

Both of these two sources are single objects in their classes, if one does not count the multiclass objects. Proplyd 245-502 (blue in Figs A10a and b) is proplyd 206-446 (Figs A9c and d) is associated with a microjet perpendicular to the disc and faces θ^2 Ori A (Bally et al. 2000), and although we are again limited by spatial resolution, the MUSE data seem to hint that this proplyd might have an SLHI component.

⁴ We will not discuss proplyds 231-502, 231-460, 232-455 and 221-443, as the former three are too close to θ^2 Ori A to be properly distinguished, and the latter is confused with the emission coming from the BB.

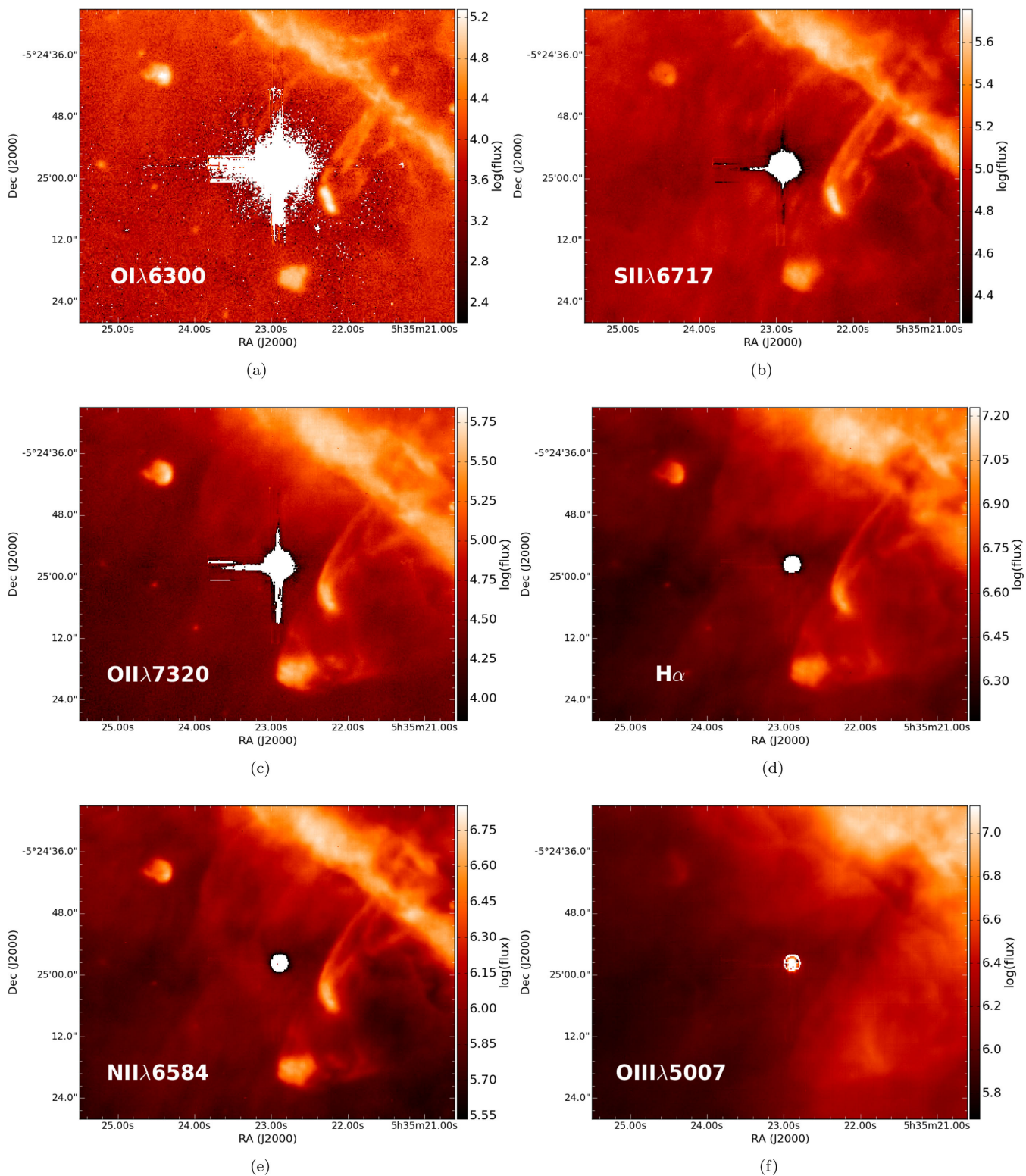


Figure 17. Continuum-subtracted integrated intensity maps of HH203 and 204, as well as 244–440 [O I] $\lambda 6300$ (a), [S II] $\lambda 6717$ (b), [O II] $\lambda 7320$ (c), H α (d), [N II] $\lambda 6584$ (e) and [O III] $\lambda 5007$ (f). The flux is measured in 10^{-20} erg s $^{-1}$ cm $^{-2}$ pixel $^{-1}$, all maps are linearly scaled to minimum/maximum.

6 CONCLUSIONS

An analysis of the Orion nebula in terms of ionic and total abundances as well as kinematics of the ionized gas was presented, based on optical integral field observations with the instrument

MUSE@VLT. The following points summarize the main results of this paper.

- (i) The first 5 arcmin \times 6 arcmin ionic and total abundance maps of oxygen, sulphur and nitrogen of the Orion nebula are presented.

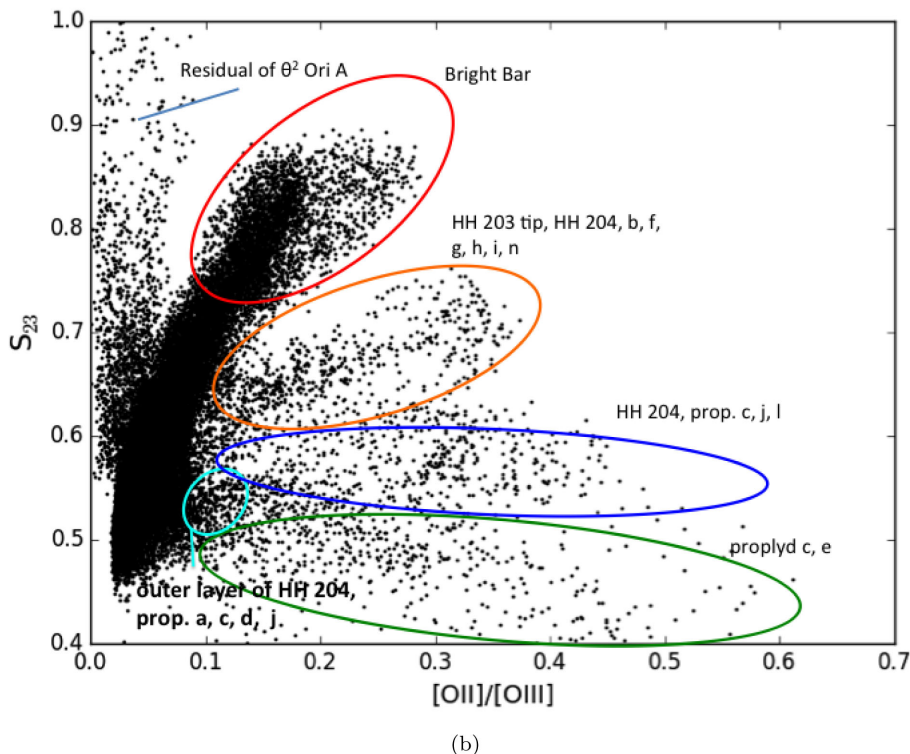
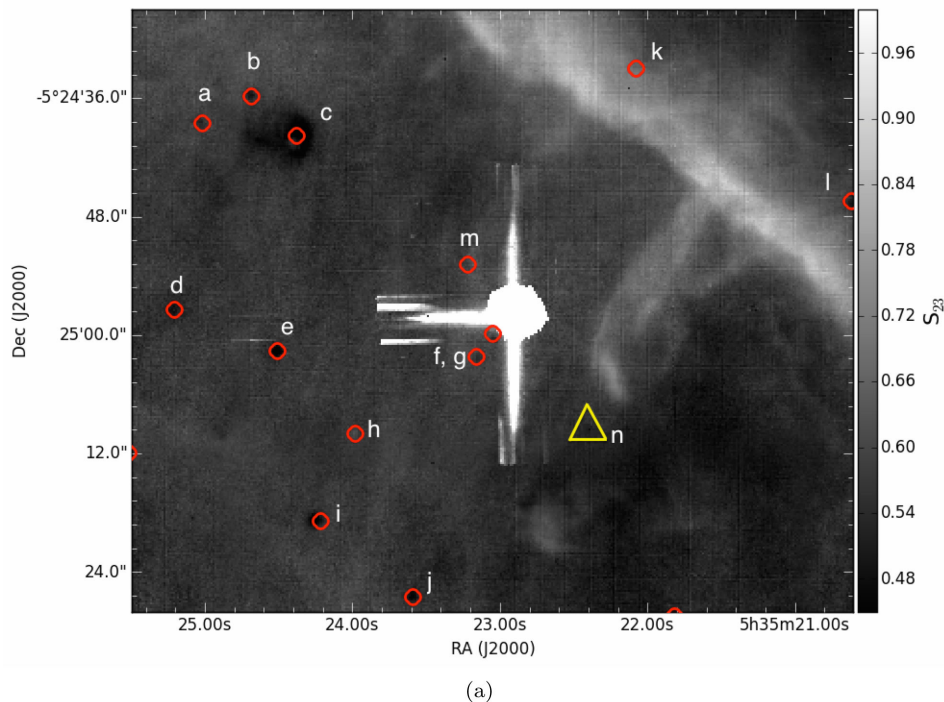


Figure 18. S_{23} map of the region containing the Herbig–Haro objects HH203, 204 as well as the proplyd Orion 244–440 (panel a), red circles and letters from *a* to *m* indicate the Orion proplyds in this field, the yellow triangle indicated with the letter *n* marks the position of a candidate proplyd (see text Section 5.2 and Table 5). Panel (b): S_{23} versus $[O\ II]/[O\ III]$ parameter space of the same region. Strong residuals of θ^2 Ori A from the continuum-subtraction are indicated in panel (b).

(ii) The abundance maps are contaminated by a certain degree of structuring that traces the main features of M 42 (the BB, the Orion S regent, HH 203 and 204, some of the proplyds). Furthermore, the ionic abundances computed from the MUSE data do not agree with literature values. We suggest that a combination of observational

limitations (e.g. high level of noise in the electron temperature and $[O\ II]$ maps, strong dependence of the abundances on the physical parameters) and intrinsic properties (e.g. high-density regions with densities approaching the critical values of the species used to compute the physical parameters) lead to the described discrepancies

Table 5. Orion proplyds. The proplyd Id linking to Fig. 18 (column 1), the proplyd number from Ricci et al. (column 2), the coordinates (J2000, column 3), and the type (column 4, i = ionized disc seen in emission, J = jet, B = binary system, mj = microjet, SLLI = S_{23} -low and low ionization, SLHI = S_{23} -low and high ionization, MSLI = medium S_{23} values and low ionization, SHLI = S_{23} -high and low ionization).

Id	Object	Coordinates	Type ^a
a	250-439	5 35 25.02 – 5 24 38.49	i, SLHI
b	247-436	5 35 24.69 – 5 24 35.74	i, J, SHLI, mj
c	244-440	5 35 24.38 – 5 24 39.74	i, SLHI + MSLI (out), SLLI (middle), MSLI (disc), mj
d	252-457	5 35 25.21 – 5 24 57.34	i, SLHI, mj
e	245-502	5 35 24.51 – 5 25 01.59	i, SLLI
f	231-502	5 35 23.16 – 5 25 02.19	i, B, SHLI
g	231-460	5 35 23.05 – 5 24 59.58	i, SHLI
h	239-510	5 35 23.98 – 5 25 09.94	i, SHLI
i	242-519	5 35 24.22 – 5 25 18.79	i, SHLI, mj
j	236-527	5 35 23.59 – 5 25 26.54	i, SLHI + MSLI
k ^b	221-433	5 35 22.08 – 5 24 32.95	i
l	206-446	5 35 20.62 – 5 24 46.45	i, MSLI, mj
m ^b	232-455	5 35 23.22 – 5 24 52.79	i
n ^c	224-510	5 35 22.41 – 5 25 09.61	SHLI

Notes: ^aFrom Ricci et al. (2008), this work and Bally et al. 2000.

^bNon-detection in this work.

^cNew detection from this work.

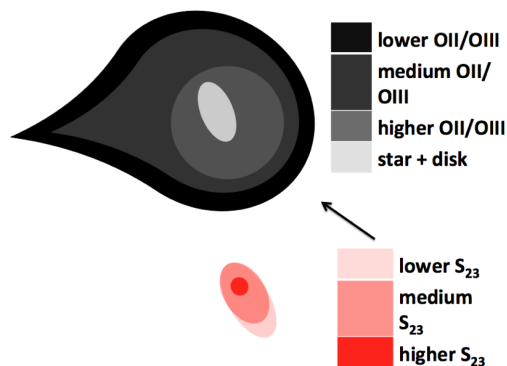


Figure 19. Sketch of Orion 244-440: the outer layer displays an $[O\ II]/[O\ III]$ gradient with decreasing ionization from the outside in (grey-scale in upper figure), the star+disc component (lower figure) shows an S_{23} gradient which increases away from the direction of motion. The black arrow indicates the direction of θ^2 Ori A.

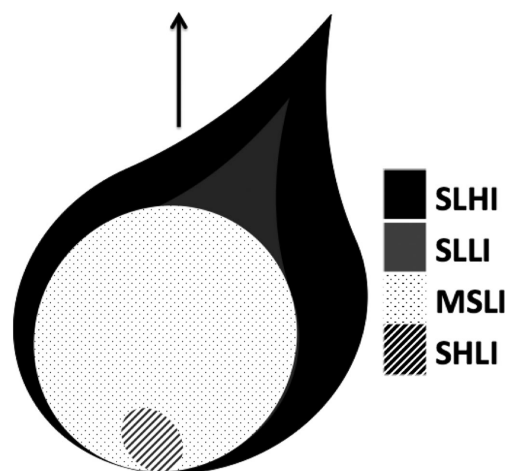


Figure 20. Sketch of HH204. The black arrow indicates the direction to θ^2 Ori A, while the direction of motion is along the head–tail axis.

between previously published data and this work. Within errors, the computed O and S abundances are in agreement with literature values.

(iii) The computed structure functions (S_2) prove that this data set lacks the depth to reproduce previous results, which showed that in the Orion nebula, the slope of S_2 corresponds to a broken power law with a steeper index at small scales and a turnover to a shallower index at larger scales. The structure functions computed in this work are much shallower than previous results, as they are highly affected by the large number of pixels with low S/N in the velocity maps. We demonstrated how noise can affect the structure function with simulated $H\ II$ regions, and will discuss this issue in depth in a forthcoming paper.

(iv) The only HH object that stands out from the rest is HH 201, the only one of the so called Orion bullets covered by the MUSE mosaic. This outflow, similarly to the one identified in our analysis about the Pillars of Creation, shows very high S_{23} together with a very high degree of ionization. From previous studies it seems that this object originates from an explosive event that occurred in the BN-KL star-forming region. Based on its cometary shape in the velocity maps and on the double component seen in the $[Fe\ II]$ line, we speculate that this object is currently impacting in a region with high densities and that is therefore currently being disrupted.

(v) We applied a method developed in our previous publication about the iconic Pillars of Creation in M 16 to the Orion data set to analyse the outflows and proplyds. In this method, the S_{23} parameter is analysed in terms of the corresponding degree of ionization (given by the ratio $[O\ II]/[O\ III]$). We find that the proplyds can be divided into two distinct populations, in correlation with their location. The population of proplyds near the Trapezium cluster have lower S_{23} values and a higher degree of ionization, while the population of proplyds that lie south of the BB seem to be more shielded from the intense feedback of the Trapezium stars, as they show higher S_{23} values and lower degree of ionization. Furthermore, the proplyds and HH objects south of the Bar can be in turn divided into four classes, depending on their S_{23} versus $[O\ II]/[O\ III]$ values, and we show how they can be clearly distinguished in the S_{23} versus $[O\ II]/[O\ III]$ parameter space. This demonstrates that this method

is very useful to pick out these kind of objects in the S_{23} versus $[O\text{ II}]/[O\text{ III}]$ parameter space.

(vi) We suggest that the reason for the capability of the S_{23} parameter to distinguish between the BB, the HH outflows and the proplyds is twofold: this line ratio traces both high degrees of ionization (given by the higher S_{23} values) and the relative contribution of shocks to the excitation mechanism (in the regime of low S_{23} values).

ACKNOWLEDGEMENTS

This work is based on MUSE commissioning data obtained with ESO telescopes at the Paranal Observatory under programme 60.A-9100(A). The data reduction and analysis make use of APLPY (<http://aplpy.github.io>), SPECTRAL_CUBE (spectral-cube.readthedocs.org), PYSPECKIT (pyspeckit.bitbucket.org), Ginsburg & Mirocha (2011) and GLUE (glueviz.org). This research was supported by the Christiane Nüsslein-Volhard Foundation (AFMCL) and the DFG cluster of excellence *Origin and Structures of the Universe* (JED). PMW received funding through BMBF Verbundforschung (project MUSE-AO, grant 05A14BAC). This work was partly supported (LT) by the Italian Ministero dell'Istruzione, Università e Ricerca through the grant *Progetti Premiali 2012 – iALMA* (CUP C52I13000140001).

REFERENCES

- Aggarwal K. M., Keenan F. P., 1999, *ApJS*, 123, 311
 Bacon R. B. et al., 2014, *The Messenger*, 157, 13
 Baldwin J. A., Ferland G. J., Martin P. G., Corbin M. R., Cota S. A., Peterson B. M., Slettebak A., 1991, *ApJ*, 374, 580
 Bally J., O'Dell C. R., McCaughrean M. J., 2000, *AJ*, 119, 2919
 Bally J., Ginsburg A., Silvia D., Youngblood A., 2015a, *A&A*, 579, A130
 Bally J., Ginsburg A., Silvia D., Youngblood A., 2015b, *A&A*, 579A, 130
 Blagrove K. P. M., Martin P. G., Baldwin J. A., 2006, *ApJ*, 644, 1006
 Boneberg D. M., Dale J. E., Girichidis P., Ercolano B., 2015, *MNRAS*, 447, 1341
 Castaneda H. O., 1988, *ApJS*, 67, 93
 Chakraborty A., Anandarao B. G., 1999, *A&A*, 346, 947
 Dale J. E., Ercolano B., Bonnell I. A., 2013, *MNRAS*, 430, 234
 Ercolano B., Barlow M. J., Storey P. J., Liu X.-W., 2003, *MNRAS*, 340, 1136
 Ercolano B., Barlow M. J., Storey P. J., 2005, *MNRAS*, 362, 1038
 Ercolano B., Young P. R., Drake J. J., Raymond J. C., 2008, *ApJS*, 175, 534
 Esteban C., Peimbert M., Torres-Peimbert S., Escalante V., 1998, *MNRAS*, 295, 401
 Esteban C., Peimbert M., García-Rojas J., Ruiz M. T., Peimbert A., Rodríguez M., 2004, *MNRAS*, 355, 229 (E04)
 Galavis M. E., Mendoza C., Zeppen C. J., 1997, *A&AS*, 123, 159
 García-Benito R. et al., 2010, *MNRAS*, 408, 2234
 Ginsburg A., Mirocha J., 2011, *Astrophysics Source Code Library*, record ascl:1109.001
 Graham M. F., Meaburn J., Redman M. P., 2003, *MNRAS*, 343, 419
 Hägele G. F., Díaz Á. I., Terlevich E., Terlevich R., Pérez-Montero E., Cardaci M. V., 2008, *MNRAS*, 383, 209
 Henney W. J., O'Dell C. R., 1999, *AJ*, 118, 2350
 Kolmogorov A., 1941, *Dokl. Akad. Nauk SSSR*, 30, 301
 Lagrois D., Joncas G., 2011, *MNRAS*, 413, 721
 McLeod A. F., Dale J. E., Ginsburg A., Ercolano B., Gritschneider M., Ramsay S., Testi L., 2015, *MNRAS*, 450, 1057 (MC15)
 Medina Tanco G. A., Sabalisk N., Jatenco-Pereira V., Opher R., 1997, *ApJ*, 487, 163
 Mesa-Delgado A., Esteban C., García-Rojas J., 2008, *ApJ*, 675, 389

- Mesa-Delgado A., Núñez-Díaz M., Esteban C., López-Martín L., García-Rojas J., 2011, *MNRAS*, 417, 420 (MD11)
 Miville-Deschenes M.-A., Joncas G., Durand D., 1995, *ApJ*, 454, 316
 Núñez-Díaz M., Mesa-Delgado A., Esteban C., López-Martín L., García-Rojas J., Luridiana V., 2012, *MNRAS*, 421, 3399
 O'Dell C. R., 1986, *ApJ*, 304, 767
 O'Dell C. R., 2001, *ARA&A*, 39, 99
 O'Dell C. R., Wen Z., 1992, *ApJ*, 387, 229
 O'Dell C. R., Wen Z., 1994, *ApJ*, 436, 194
 O'Dell C. R., Wen Z., Hu X., 1993, *ApJ*, 410, 696
 Osterbrock D. E., Tran H. D., Veilleux S., 1992, *ApJ*, 389, 305
 Parenago P. P., 1954, *Tr. Gos. Astron. Inst.*, 25, 1
 Peimbert M., 1967, *ApJ*, 150, 825
 Peimbert M., Torres-Peimbert S., 1977, *MNRAS*, 179, 217
 Podobedova L. I., Keller D. E., Wiese W. L., 2009, *J. Phys. Chem. Ref. Data*, 38, 171
 Pradhan A. K., Montenegro M., Nahar S. N., Eissner W., 2006, *MNRAS*, 366, L6
 Ricci L., Robberto M., Soderblom D. R., 2008, *AJ*, 136, 2136
 Rubin R. H., Dufour R. J., Walter D. K., 1993, *ApJ*, 413, 242
 Sánchez S. F., Cardiel N., Verheijen M. A. W., Martín-Gordón D., Vilchez J. M., Alves J., 2007, *A&A*, 465, 207
 Schlafly E. F. et al., 2014, *ApJ*, 786, 29
 Storey P. J., Zeppen C. J., 2000, *MNRAS*, 312, 813
 Tayal S. S., 2007, *ApJS*, 171, 331
 Tayal S. S., 2011, *ApJS*, 195, 12
 Tayal S. S., Gupta G. P., 1999, *ApJ*, 526, 544
 Tayal S. S., Zatsarinny O., 2010, *ApJS*, 188, 32
 Tedds J. A., Brand P. W. J. L., Burton M. G., 1999, *MNRAS*, 307, 337
 van Altena W. F., Lee J. T., Lee J.-F., Lu P. K., Uppgren A. R., 1988, *AJ*, 95, 1744
 Vilchez J. M., Esteban C., 1996, *MNRAS*, 280, 720
 von Hoerner S., 1951, *Z. Astrophys.*, 30, 17
 Weibacher P. M., Streicher O., Urrutia T., Jarno A., Pécontal-Rousset A., Bacon R., Böhm P., 2012, in Radziwill N. M., Chiozzi G., eds, *Proc. SPIE Conf. Ser. Vol. 8451, Software and Cyberinfrastructure for Astronomy II. SPIE, Bellingham*, p. 84510B
 Weibacher P. M. et al., 2015, *A&A*, 582, 114 (W15)
 Wen Z., O'Dell C. R., 1993, *ApJ*, 409, 262
 Wiese W. L., Fuhr J. R., Deters T. M., 1996, *Atomic Transition Probabilities of Carbon, Nitrogen, and Oxygen: A Critical Data Compilation*. AIP Press, NY
 Zeppen C. J., 1982, *MNRAS*, 198, 111

APPENDIX A

Fig. A1 shows the velocity maps masked according to the $[O\text{ I}]\lambda 6300$ intensity threshold of $\sim 10^{-16}$ erg s $^{-1}$ cm $^{-2}$ pixel $^{-1}$ used to compute the second-order structure function S_2 . The effect of adding Gaussian noise to the synthetic velocity maps (Figs A2 and A3) of a simulated H II region (Fig. A6) is shown in Figs A4 and A5, where the structure functions for different values of the standard deviation σ are shown. See text Section 5.

Fig. A7 shows the equivalent of Fig. 18b, but for $[S\text{ II}]/H\beta$ (see text Section 5.2). Figures from A8–A11 show the S_{23} maps (left-hand panels) and their corresponding location in the S_{23} versus $[O\text{ II}]/[O\text{ III}]$ parameter space of the Orion proplyds listed in Table 5 and discussed in Section 5.2. Figures from A8 to A11 are intentionally not continuum-subtracted (a version of continuum-subtracted S_{23} versus $[O\text{ II}]/[O\text{ III}]$ parameter space is shown in Fig. 18) to highlight the stellar components of the proplyds (244-440, 242-519 and 247-436).

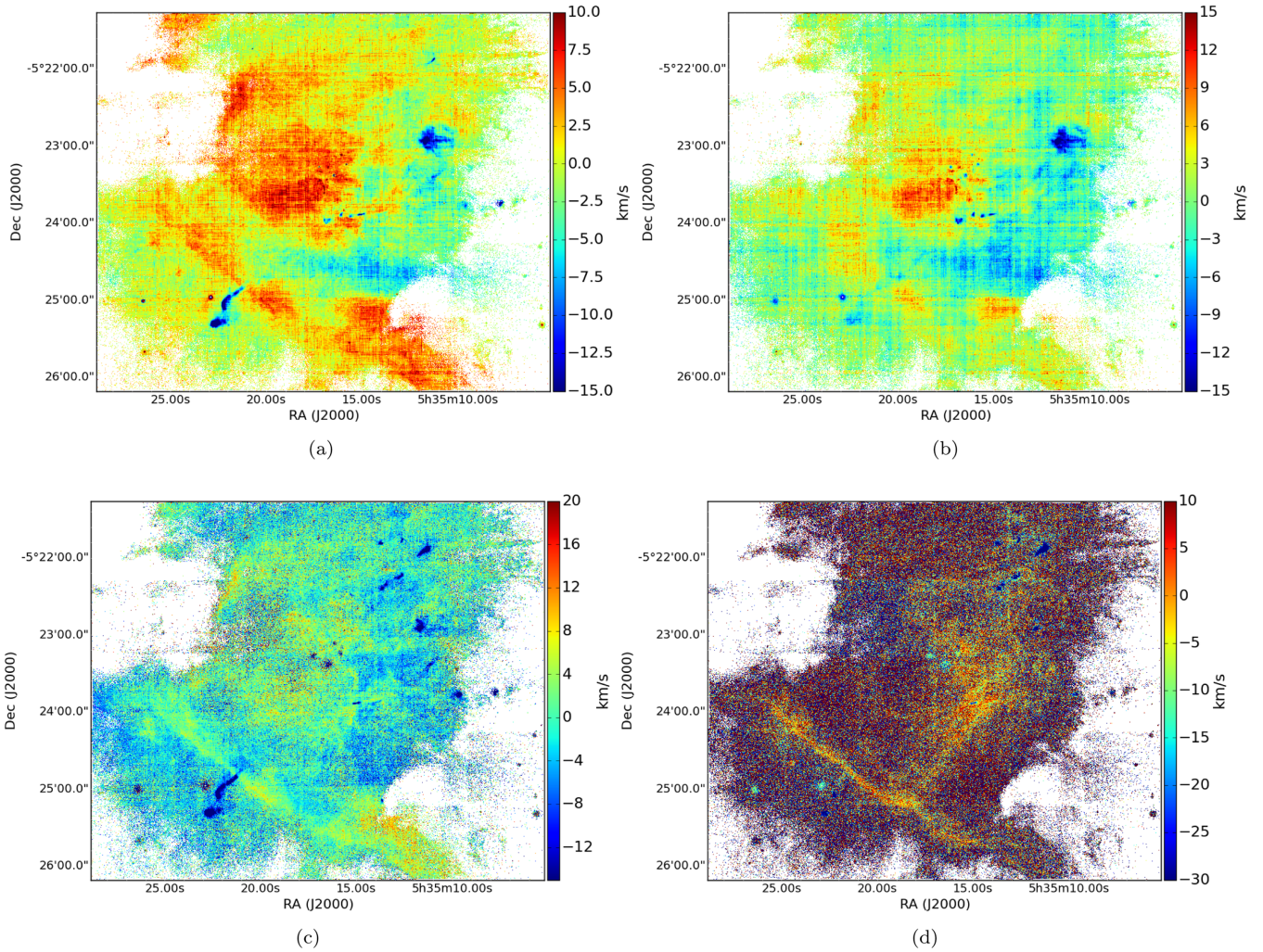


Figure A1. Velocity maps of H α (a), [O III] λ 5007 (b) and [S II] λ 6731 (c) and [O I] λ 6300 (d) masked based on the mean value of the [O I] line. The indicated velocities correspond to velocities relative to the mean velocity of the surrounding medium (see text Section 5.1).

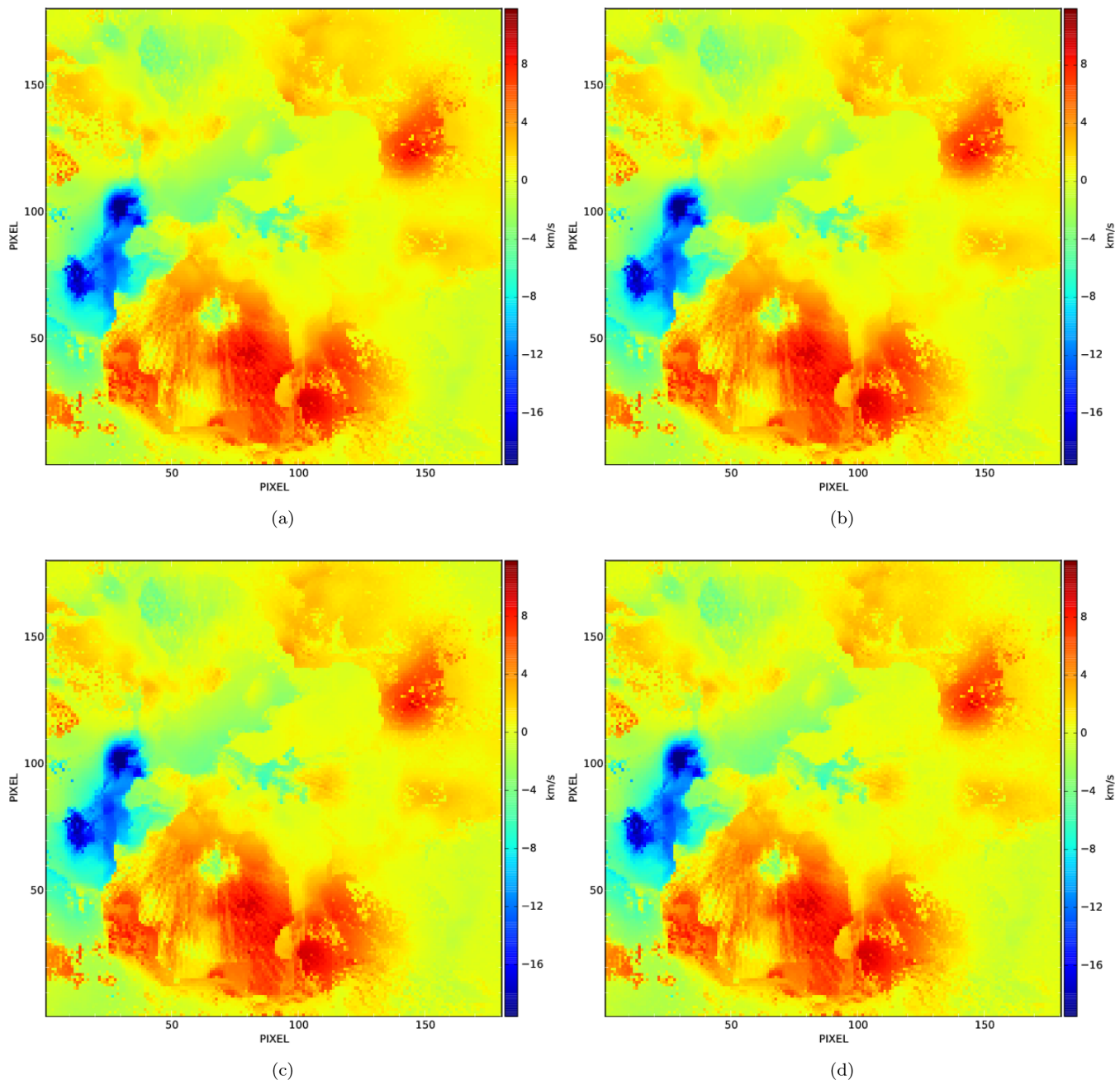


Figure A2. [S II] velocity map of our simulated H II region (panel a), post-processed with the ionization radiative transfer code MOCASSIN. The pixel scale is 0.028 pc. To this we gradually add Gaussian noise by increasing the standard deviation σ from 0.01 km s⁻¹ (panel b) to 10 (panel d in Fig. A3).

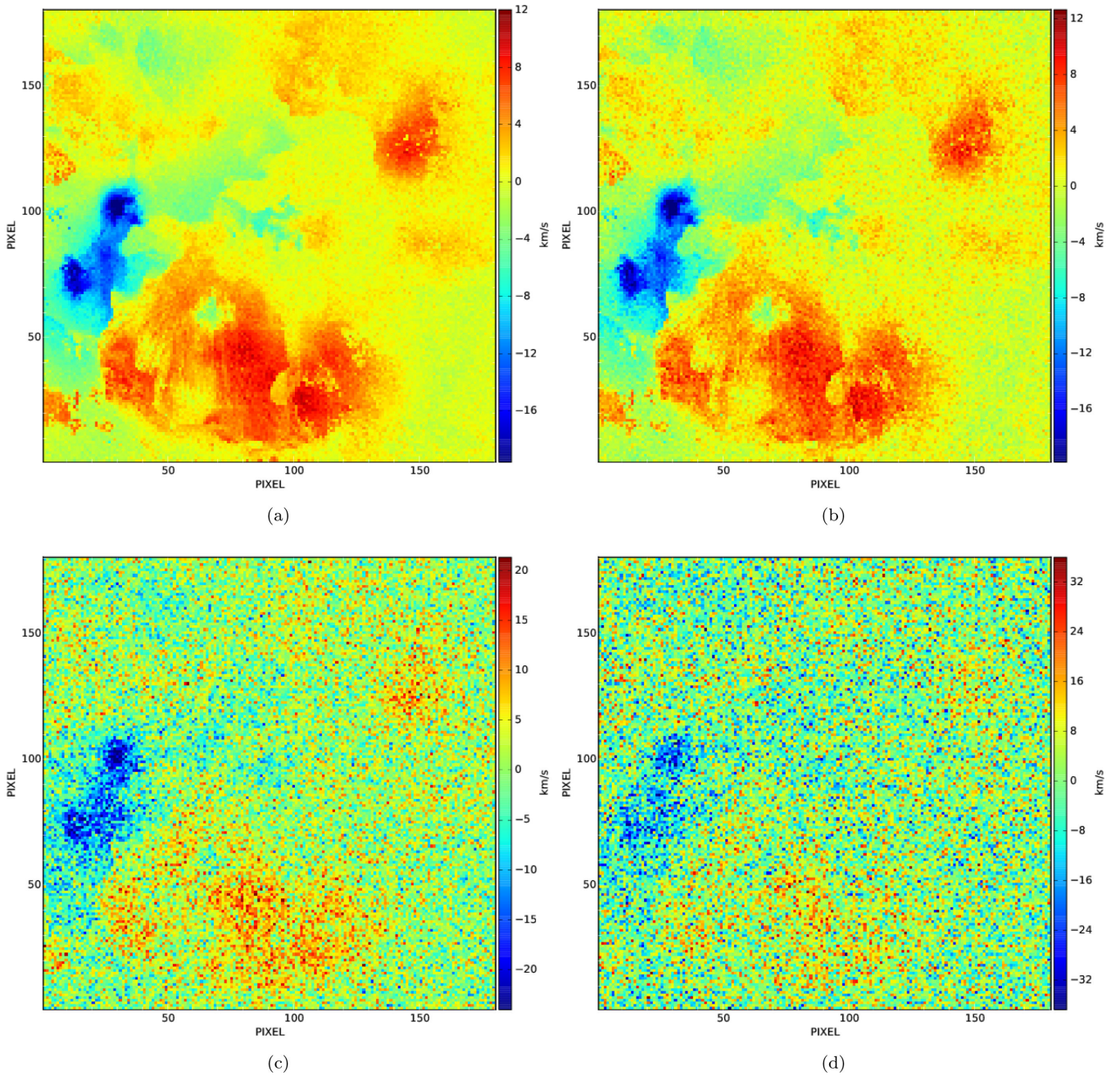


Figure A3. See Fig. A2.

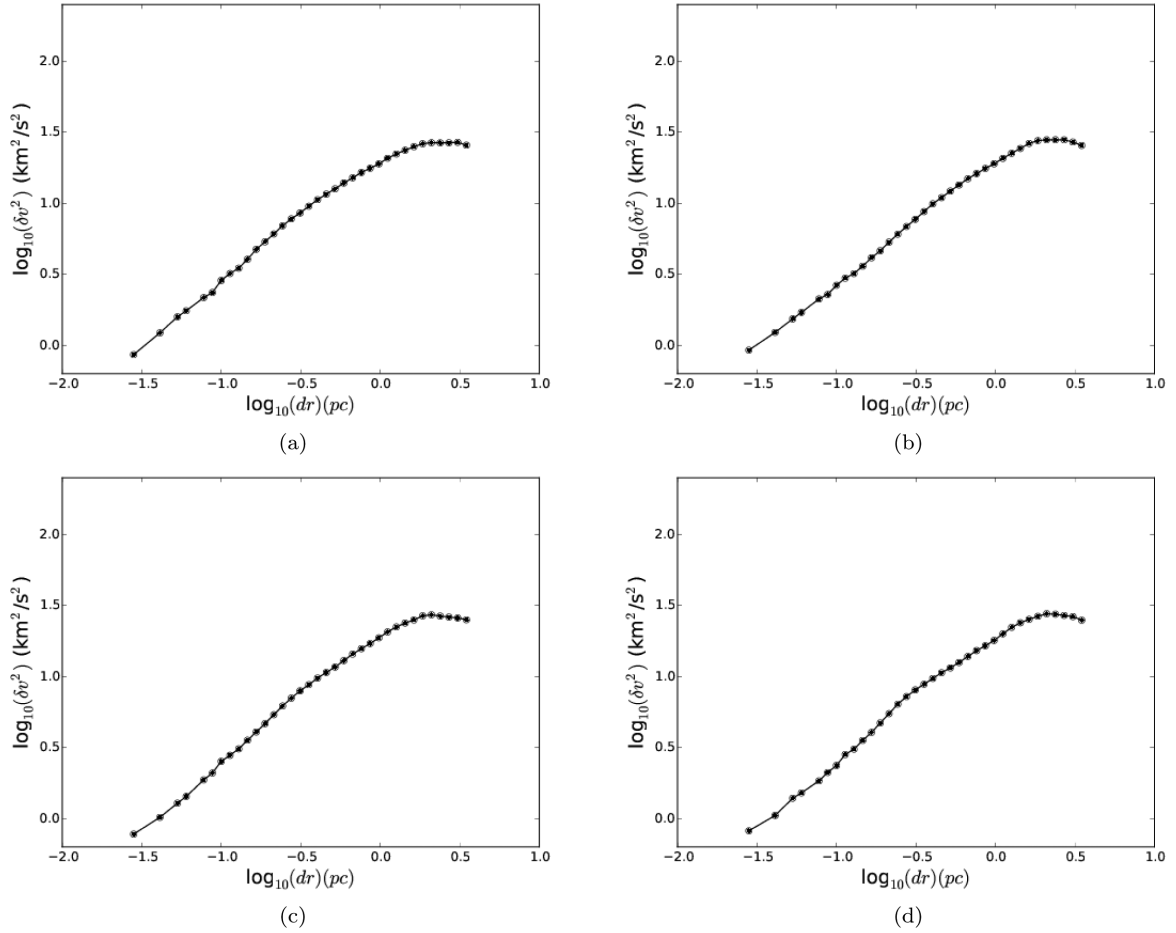


Figure A4. Structure function corresponding to the [S II] velocity map of our simulated H II region (panel a). To this we gradually add Gaussian noise by increasing the standard deviation σ from 0.01 km s^{-1} (panel b) to 10 (panel d in Fig. A5). To show the flattening of the structure function, all plots share the same scaling.

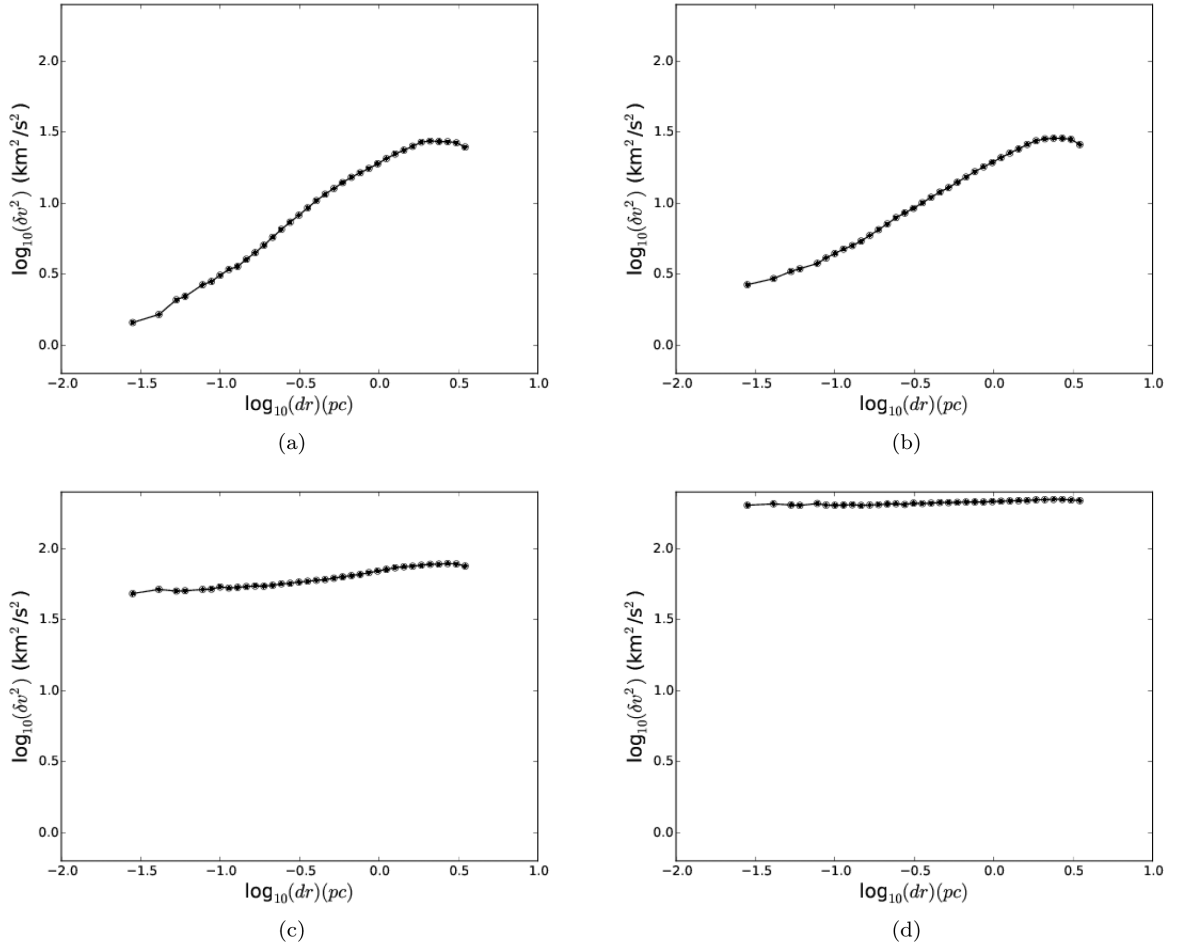


Figure A5. See Fig. A4.

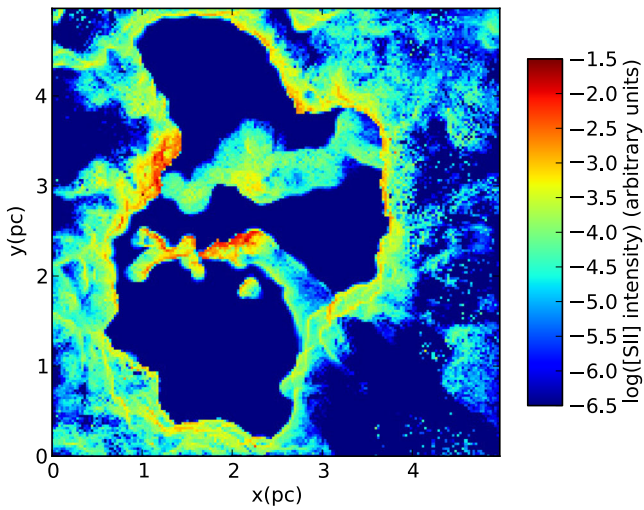


Figure A6. Integrated [S II] intensity map of the synthetic star-forming molecular cloud, post-processed with MOCASSIN. See text Section 4.

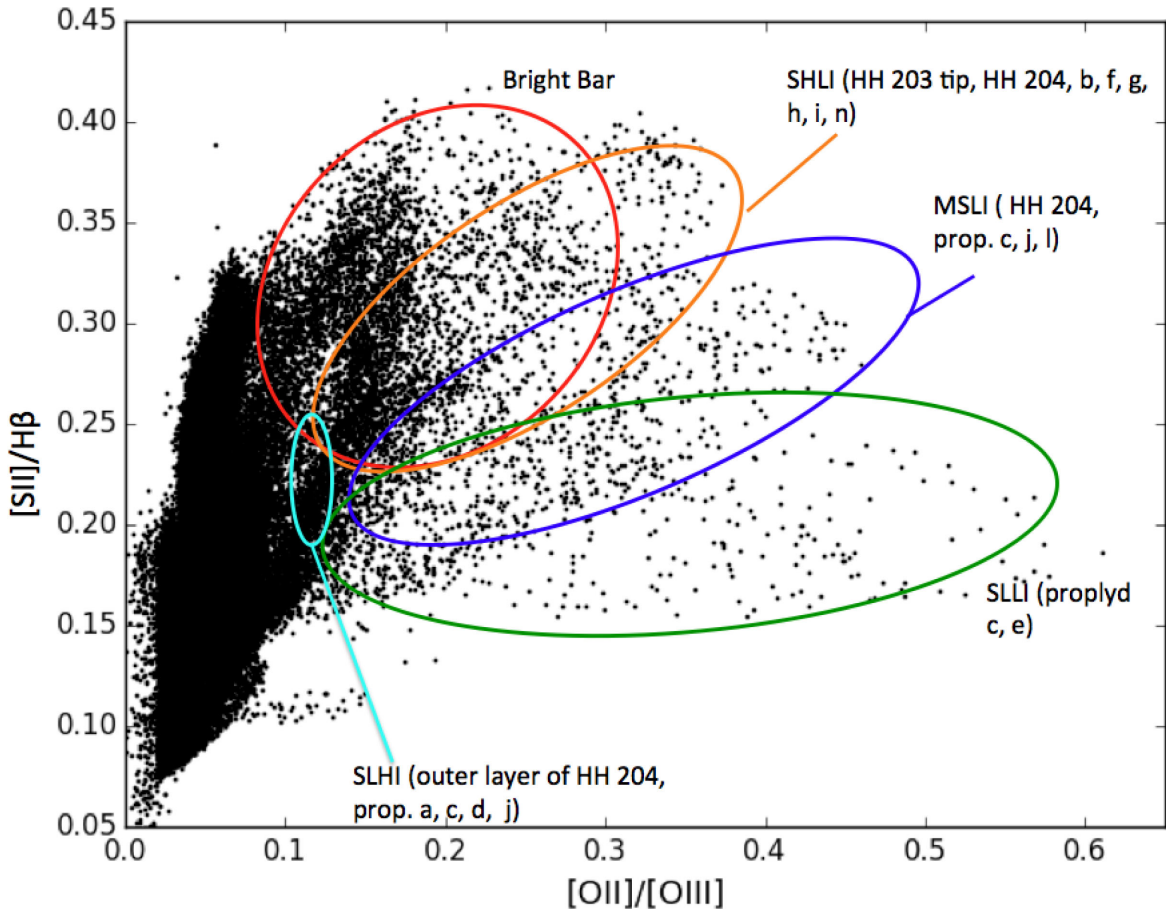


Figure A7. $[S II]/H\beta$ versus $[O II]/[O III]$ scatter plot, with the same regions as indicated in Fig. 18(b). See text Section 5.2.

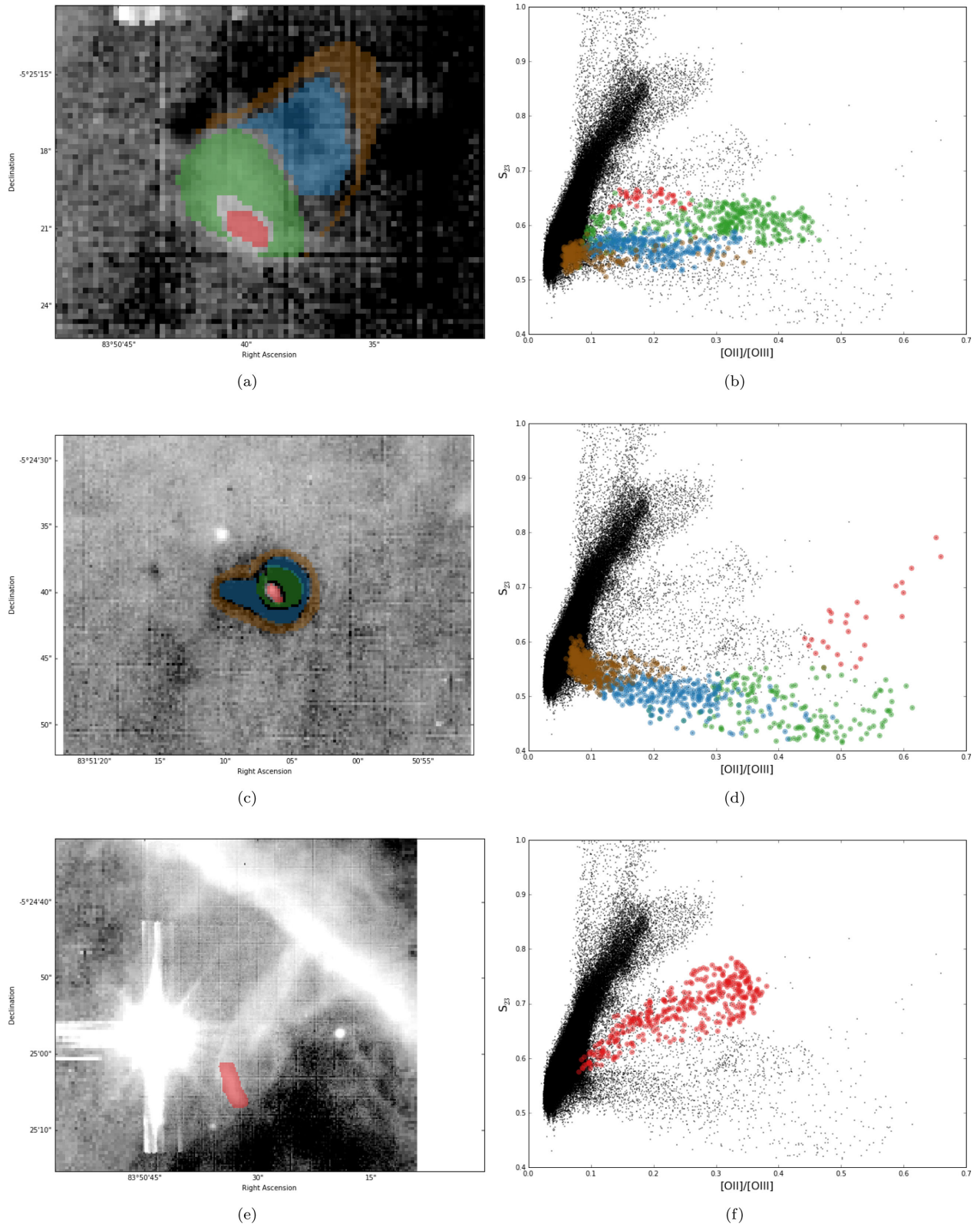


Figure A8. S_{23} maps (left-hand panels) and S_{23} versus $[O\text{II}]/[O\text{III}]$ scatter plots (right-hand panels) of HH 204 (panels a and b), proplyd 244-440 (panels c and d) and HH 203 (panels e and f). Scales and coordinates are the same as in Fig. 18.

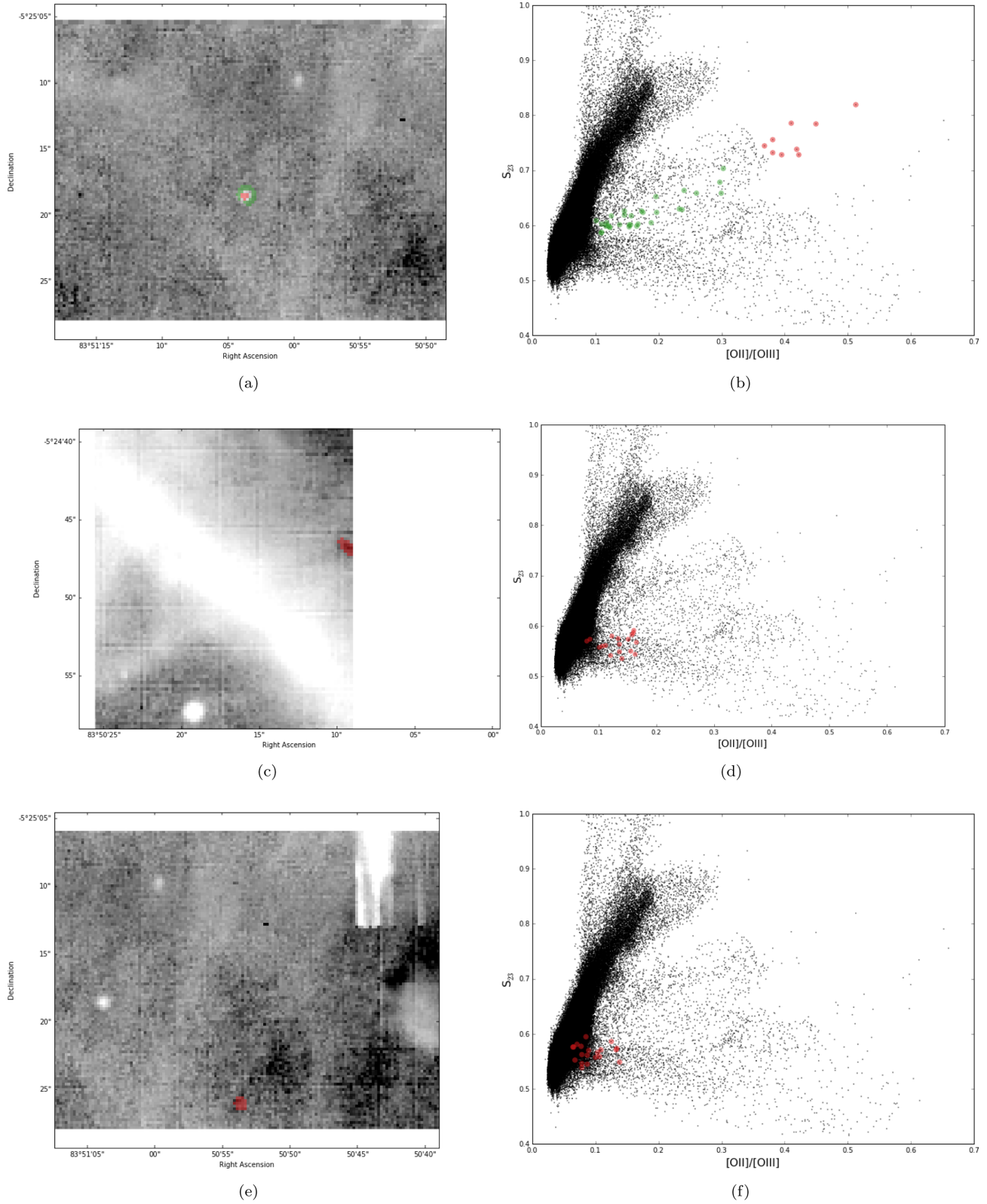


Figure A9. Same as Fig. A8, but for proplyds 242-519 (panels a and b), 206-446 (panels c and d) and 236-527 (panels e and f).

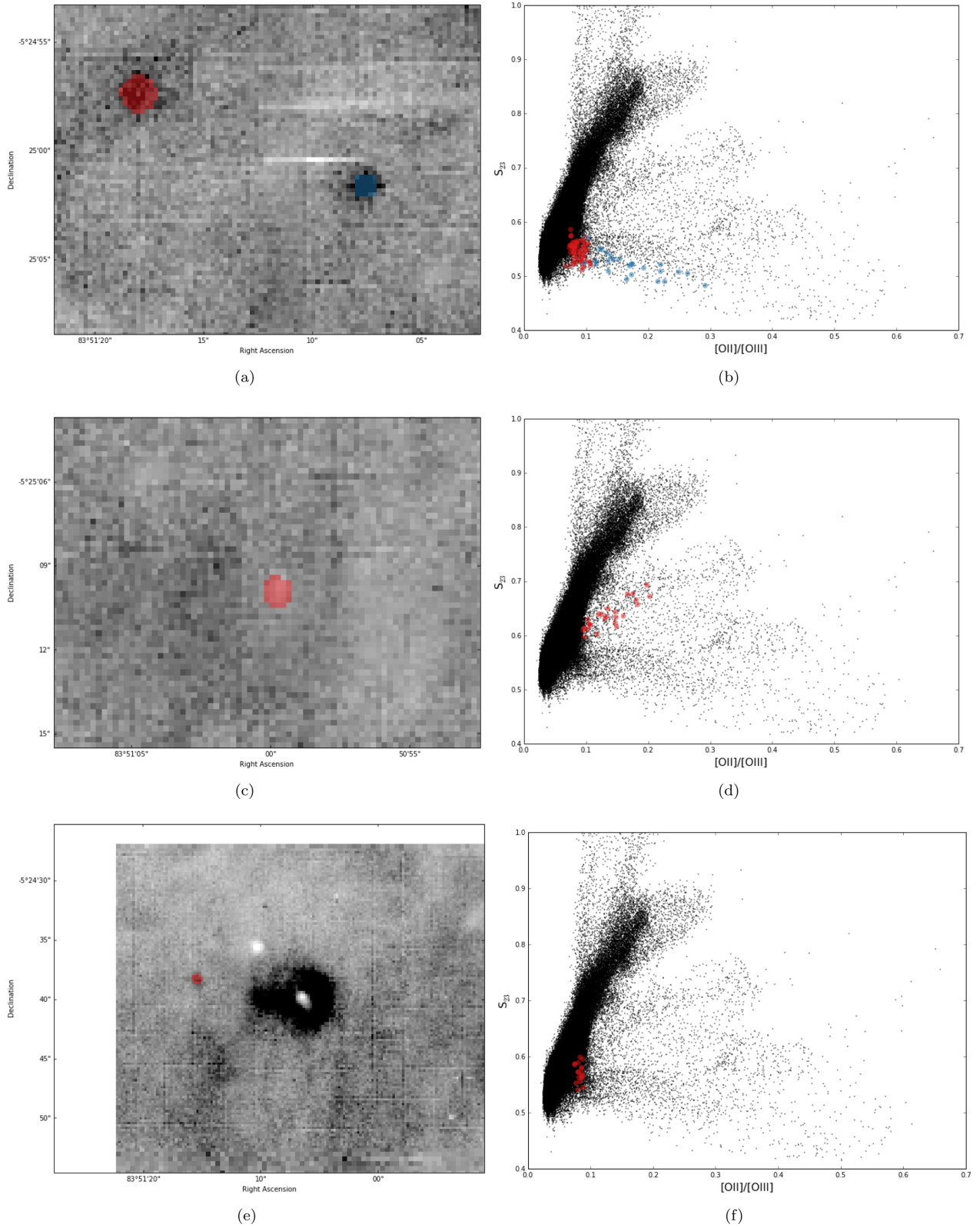


Figure A10. Same as Fig. A8, but for the proplyds 252-457 and 245-502 (red and blue, respectively, in panels a and b), 239-510 (panels c and d) and 250-439 (panels e and f).

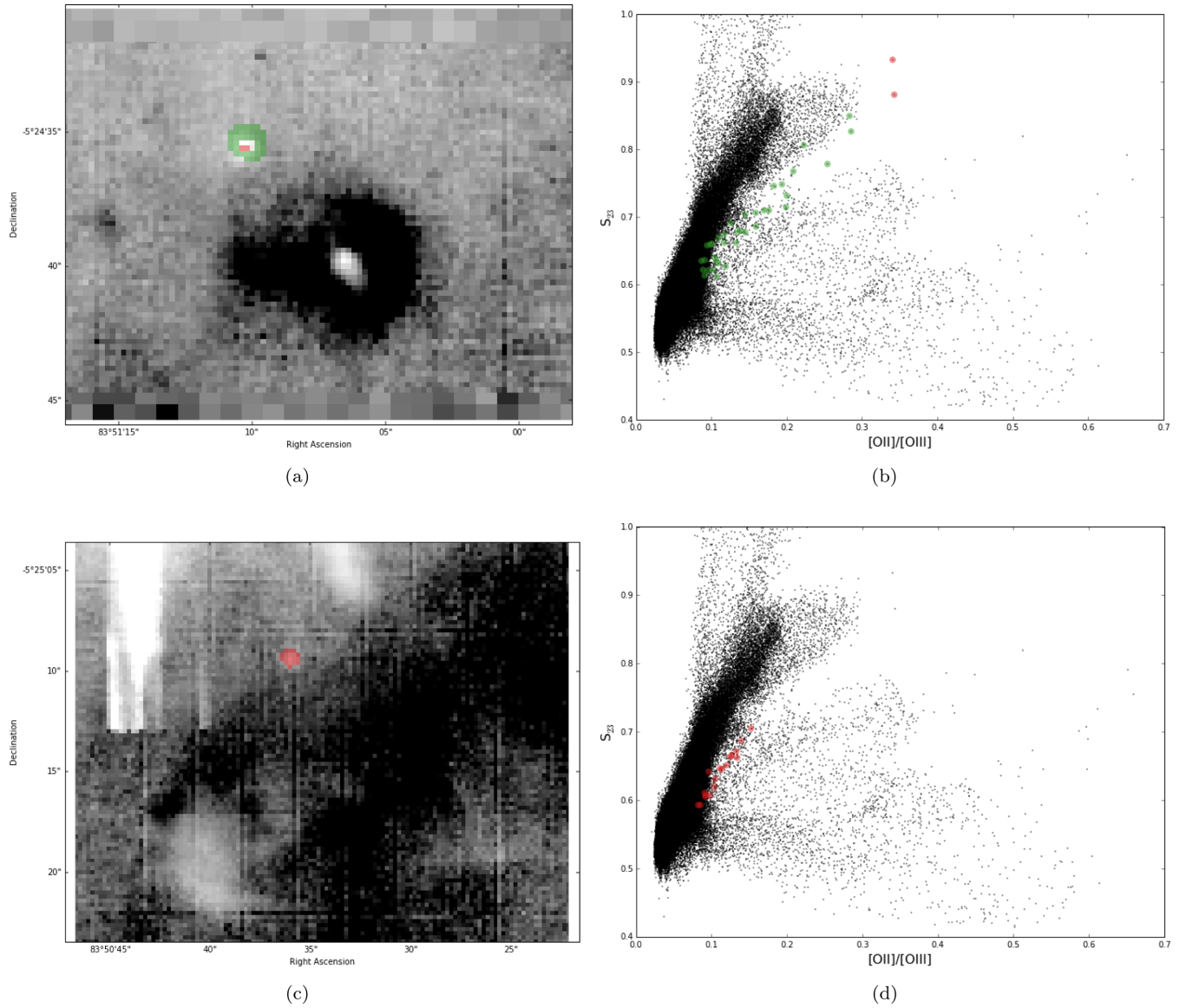


Figure A11. Same as Fig. A8, but for the propylid 247-436 (panels a and b), the candidate propylid (224-510, letter *n* in Fig. 18a, panels c and d).

This paper has been typeset from a $\text{\TeX}/\text{\LaTeX}$ file prepared by the author.